Supplementary Materials for:

Faulting of Rocks in a Three-Dimensional Stress Field by Micro-Anticracks

H.O. GHAFFARI[1], M.H.B. NASSERI [1]& R.PAUL YOUNG [1]

[1] *Department of Civil Engineering and Lassonde Institute, University of Toronto, Toronto, 170 college street ,M5S3E3,ON, Canada*

[1] . h.o.ghaffari@gmail.com; MB108-170 College Street, Department of Civil Engineering and Lassonde Institute, University of Toronto, Toronto, Canada M5S3E3;

In this supplementary document, we demonstrate more evidence of our claims in the main text. In sections (I) and (II), we demonstrate a summary of experimental procedure and our employed algorithms in terms of functional acoustic-networks. The main focus of this supplementary document is on TTTs and in particular FTB4. First, we examine duration of the second phase in Q-profiles in different materials and under different conventional loading conditions. The materials in this section show that unusual rupture fronts in micron and sub-micron scales are not due to geometry of the samples or loading rate or other details of conventional loading conditions. Next, we develop a framework based on R-profiles to extract failure phase diagrams per each recorded events using sub-networks on FTB4 and other CTTs. Furthermore, using global (multiplex network) networks' phase planes and Q-profiles, we illustrate the unconventional nature of cracking in true triaxial tests. At the end, the waveforms from a multi-anvil test are analyzed to validate our assumption on unusual characteristics of TTT's rupture fronts.

I) Summary of Experimental Procedures:

Cubic-samples of the saturated Fontainebleau sandstone are loaded at the University of Toronto, in a true triaxial cell [1]. The cell can be used to measure permeability in different directions as well as to measure the heat conductivity of samples. Special attention was paid to keep the balance of loads in parallel directions to avoid possible torque. The strain rate for all axial directions was $3\times10^{-6}s^{-1}$. The waveforms were recorded using 18 piezoceramic transducers at a 10MHz sampling rate while triggered sensors are employed to detect the events a threshold of 60mv and minimum 6. Another system simultaneously and continuously records all noises from all transducers during the experiments. For conventional compressive tests, we used the results of previously reported experiments [2] while the samples are saturated and the events are chosen from precursor rupture fronts. A Fontainebleau sandstone specimen (length = 88 mm, diameter = 40 mm) was deformed inside a triaxial. A network of piezoceramic transducers (PZT) was used in10MHz sampling rate with similar criterion to the Polyaxial test to detect the events. In the supplementary document (section1 and 5) , we have -also-included the summary of other tests (and their multiplex networks attributes) on Westerly Granite samples under different loading conditions and geometry as well as smooth and rough rock-frictional interfaces [7]. In addition, we analysed multi-stationary waveforms from a Multi-anvil test (High pressure –High

temperature tests) on an olivine sample to infer the possible origin of shorter waveforms (section 5-supplemntary material).

II) Functional Multiplex Networks on Acoustic Emission Waveforms

In [7], we used functional networks as a class of recurrence networks to analyze precursor events during the evolution of frictional interfaces. Here, we use a similar algorithm on waveforms from acoustic emissions as our laboratory earthquakes in mesoscales. First we define a global or multiplex network on the cubic geometry in which it includes three main layers (X,Y and Z directions correspond to minimum, intermediate and maximum principle stress as far-field driving stress -field). The two extreme cases can be inferred [25-26]: (1) independent layers and (2) fully coupled layers. The "local sub-networks" were in the first class and we used them to investigate the attributes of each micro-crack on each layer. To build networks (both global and local), we use the following algorithm [7]:

- Normalization of waveforms in each station where the maximum amplitude of each recorded waveform –after normalization-is unit.

- Division of each time series to maximum segmentation. Then, we considered each recorded point in each waveform with the length of *T*. The *j*th segment from *i*th time series ($1 \le i \le N$) is denoted by $x^{i,j}(t)$. We put the length of each segment as unit. This essentiality takes into account? the high temporal- resolution of the systems' evolution.

- Adding edges: $x^{i,j}(t)$ is compared with $x^{k,j}(t)$ to create an edge among the aforementioned segments. If $d(x^{i,j}(t),x^{k,j}(t)) = \left\| x^{i,j}(t) - x^{k,j}(t) \right\| \le \xi$, we set $a_{ik}(j) = 1$ otherwise $a_{ik}(j) = 0$ in which $a_{ik}(j)$ is the component of the connectivity matrix.

- Threshold level (ξ): To select a threshold level, we use betweenness centrality (B.C.),which can be assumed as a measure of "load" on each node. The details of the method have been explained in [27-28], and it has been proven that using this method quantitatively is equal to using edge density.

- Increase the resolution of visualization: To decrease the sensitivity of the networks and knowing that recurrence networks–generally- reveal a good performance in a small number of nodes, we increased the size of the adjacency matrix with the simple interpolation of *d* using

cubic spline interpolation. Next, to set-up local networks (or sub-networks), for each parallel pair face in a cubic sample, a similar procedure was repeated to form a network.

The only change lay in increasing the size of the adjacency matrix with simple interpolation of $d_{sub\text{-}network}$ using cubic spline interpolation which becomes equal to the global network size (i.e., number of nodes). Then for both networks, the numbers of nodes were 18 and we kept the number of nodes as the constant value. We also used some main networks' metrics. Each node was characterized by its degree k_i and the clustering coefficient. For a given network with N nodes, the degree of the node and Laplacian of the connectivity matrix were defined by $k_i = \sum_{j=1}^{N} a_{ij}; L_{ij} = a_{ij} - k_i \delta_{ij}$ where k_i, a_{ij}, L_{ij} are the degree of i th node, elements of a symmetric adjacency matrix, and the network Laplacian matrix, respectively. The eigenvalues Λ_α are given by $\sum_{j=1}^{N} L_{ij}\phi_j^{(\alpha)} = \Lambda_\alpha \phi_i^{(\alpha)}$, in which $\phi_i^{(\alpha)}$ is the i th eigenvector of the Laplacian matrix ($\alpha = 1,\ldots,N$).. With sorting the indices $\{\alpha\}$ in decreasing order of the eigenvalues, we have: $0 = \Lambda_1 \geq \Lambda_2 \geq \ldots \geq \Lambda_N$ and we define $\lambda_{\max} = (-\Lambda_N)$ as the maximum eigenvalue of the Laplacian of the network. We also used the betweenness centrality (B.C) of a node as follows [29]:

$$B.C_i = \frac{1}{(N-1)(N-2)} \sum_{\substack{h,j \\ h\neq j, h\neq i, j\neq i}}^{N} \frac{\rho_{hj}^{(i)}}{\rho_{hj}} \qquad (1)$$

in which ρ_{hj} is the number of the shortest path between h and j ,and $\rho_{hj}^{(i)}$ is the number of the shortest path between h and j that passes i. The spatio-temporal average of B.C is indicated by $\overline{\log < B.C >}$ where <…> and bar-sign correspond to the spatial (i.e., nodes) and temporal averages, respectively. In [7], we speculate that events from saw and rough fault cut-experiments flow in $\overline{\lambda}_{\max} - \overline{\log < B.C >}^{-1}$ phase diagram with three disgusted trends, corresponding to rupture regime. In this study , furthermore, we map each event into local phase diagrams (i.e., sub-networks' phase spaces): $\overline{\lambda}_{\max}^{x,y,z} - \overline{\log < B.C >}_{x,y,z}^{-1}$.

In [7], we found out universal pattern of Q-profiles (i.e., dynamic evolutionary in each recorded event) over the acoustic emissions emitted during the evolution of frictional interfaces (Fig.S.2b). We also use the average skewness of Q-profiles as the asymmetry measure of pulse shapes which is quantified by [11]:

$$\Sigma = \frac{\frac{1}{T}\int_0^T Q(t)(t-\bar{t})^3 dt}{[\frac{1}{T}\int_0^T Q(t)(t-\bar{t})^2 dt]^{3/2}} \qquad (2)$$

in which $\bar{t} = \frac{1}{T}\int_0^T Q(t)tdt$ and $T = 408\mu s$ (i.e., duration of waveforms). Following [6,7], the first stage in Q-profiles of the functional acoustic-damage networks is the nucleation and the main deformation phase which shows the nature of rupture and energy release in the crack tip. To amplify this regime, we use the reciprocal of normalized (to the rest value) Q-profiles: R-profiles which show the resistance and strength of particles against deformation. For each sub-network, the maximum value of R-profiles –occurring in the first phase of Q-profiles- is indicated by R_i^I which is an indicator of the maximum strength in that direction .

1. More Features from the Experiments

The following is the list of the experiments that we have used to support our claims:

- **a.** True triaxial tests (TTT): Three Fontainebleau rock samples in cubic shapes (FTB2,FTB3,FTB4) were loaded at the homemade cell. In one of the tests, we did not make a complete balance of loading in X-direction (FTB3- non true triaxial test). We will show this effect in analysis of the monitored events.
- **b.** Conventional cylindrical geometry of Westerly Granite with different strain rates and geometries including fast-strain rate, AE-feedback control test, slow strain rate (4).
- **c.** Saw-cut and natural rough Granite-Granite frictional interfaces (7)
- **d.** Double shear experiments with different gouge materials (glass and angular quartz-sands) (5).
- **e.** Conventional cylindrical geometry of Fontainebleau sandstone rock samples (2) [and similar tests in R.P.Young's Lab].
- **f.** Compaction band test : with Conventional cylindrical geometry of Diemelstadt sandstone rock samples (10)
- **g.** Conventional cylindrical geometry of Basalt (9)
- **h.** Conventional cylindrical geometry of Concrete (Portland cement)(8)

i. Conventional cylindrical geometry on Westerly granite room temperature and thermally treated ~850 (different sample size from set-b).

j. High pressure-High Temperature (Multianvil test) on olivine samples (at University College London)

In Fig. S.1, we have shown more features from FTB4. We also depicted the sequence of the formation of faults' patches in association with stress-time and the second temporal derivation of strains in X,Y and Z directions. For a visualization of the fault-system, the reconstructed images of the stacked digital images (Micro-CT images) were filtered by a Hough transformation to detect features of the images (Fig.S.1.b, d).

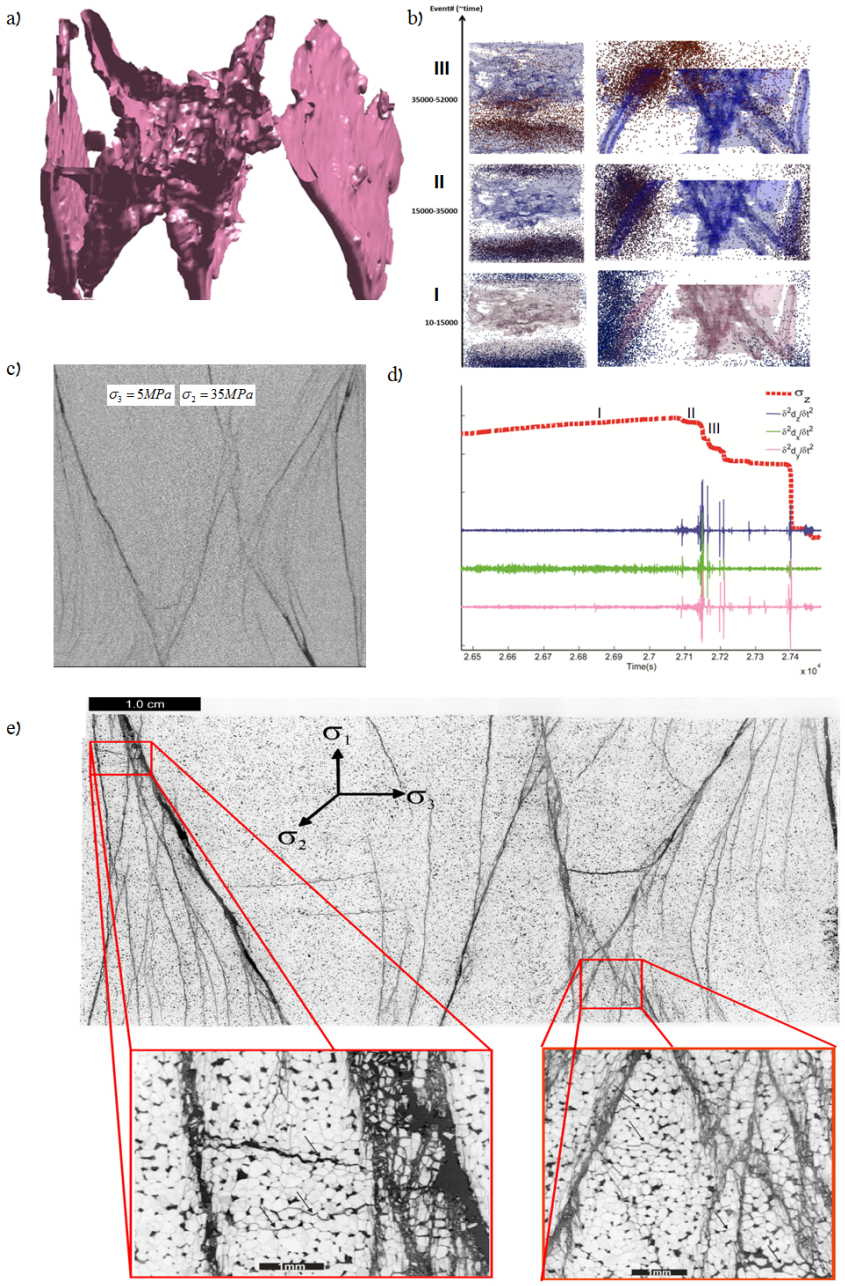

Figure S.1. a) Visualization of fault-system in the Polyaxial test-FTB4 shows the Orthorhombic faulting system. b) Superimposed events on the best-located events on the reconstructed of the X-ray patterns of the fault-system and the temporal/spatial evolution of the events (i.e., event-sets' sequences). The sequences' events for top (left) and front (right) views have been visualized. c) A cross-section of FTB4 (micro-CT image). (d) Scaled –evolution of the driving stress field (σ_z) and the second derivation of strain gauges per each direction for FTB4 test. e) Visible frequent (anti-) cracks parallel to minimum stress field in FTB4.

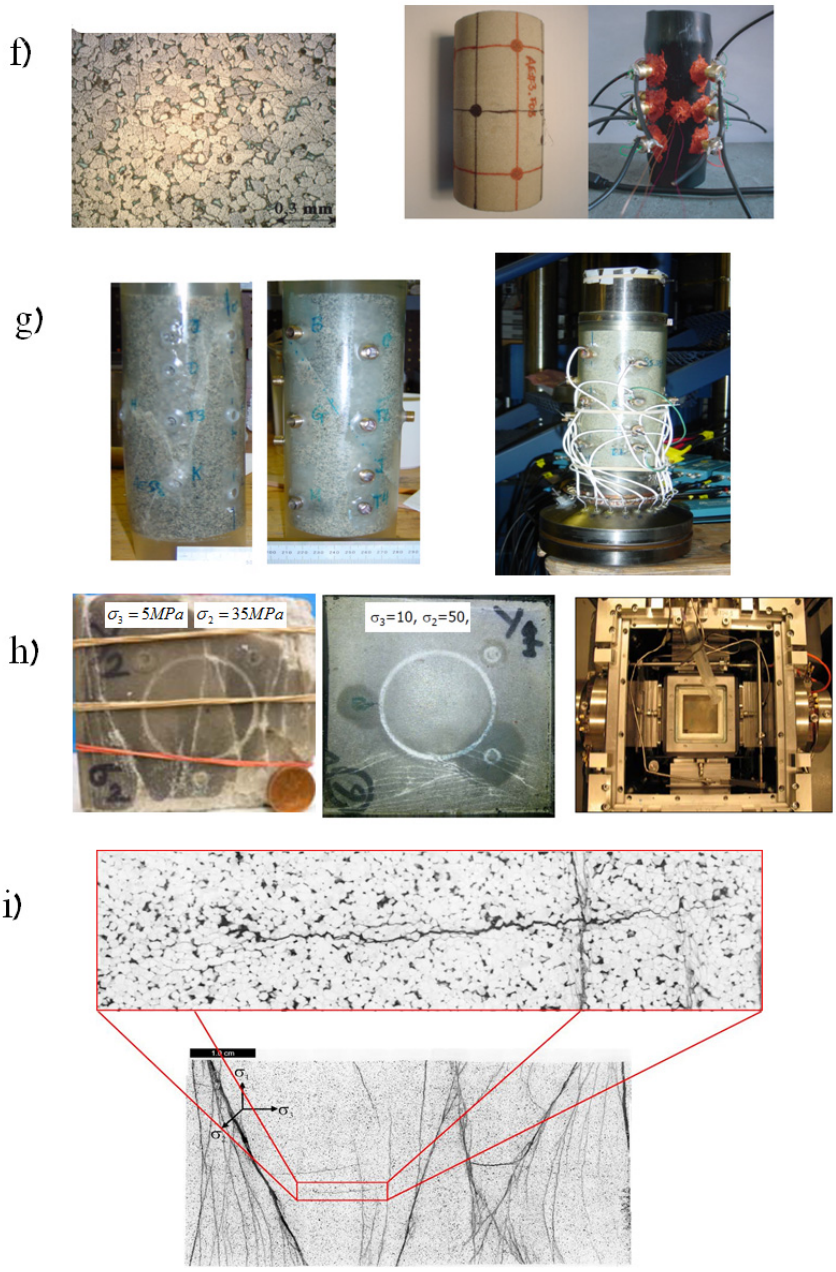

Figure.S1. (continue) –(f) fine grain Fouintblue sandstone with >90% quartz and the cylindrical sample with mounted piezoelectric sensors (data set and pictures courtesy of A.Schubnel (2)). (g) Westerly Granite samples (see Fig.S.2a-d)-data set Courtesy of B.D.Thompson. (h) The final configuration of FTB4 and FTB3 using the homemade cell to load and measure permeability (also see (1) for more information on design of the cell). (i) Developing a fast true compaction band with distinguished features of compaction crack tip-zone. Note that experimentally observed compaction bands under high confining pressures do not satisfy the conditions of true-natural bands. Thicker in the middle and thinner at the edge associated with process zone at the anti-crack tip are the characteristics of the typical anti-crack fronts.

In FigS.1f-h, we have shown three rock samples (a cylindrical Sandstone sample, Westerly Granite, and a Cubic-TTT sample) with acoustic-piezoelectric sensors set-up on them. Next, we prove the following lemma: *Under different loading condition and sample sizes, the fast-slip phase of Q-profiles do not effectively change in conventional compressive tests* (CTT-FigS.1f). To test this proposal, we use the results of different loading condition tests on Westerly Granite, reported previously in (4). The sample size for these sets of events was: 190 mm (height) and 76mm in diameter of the cylindrical rock samples.

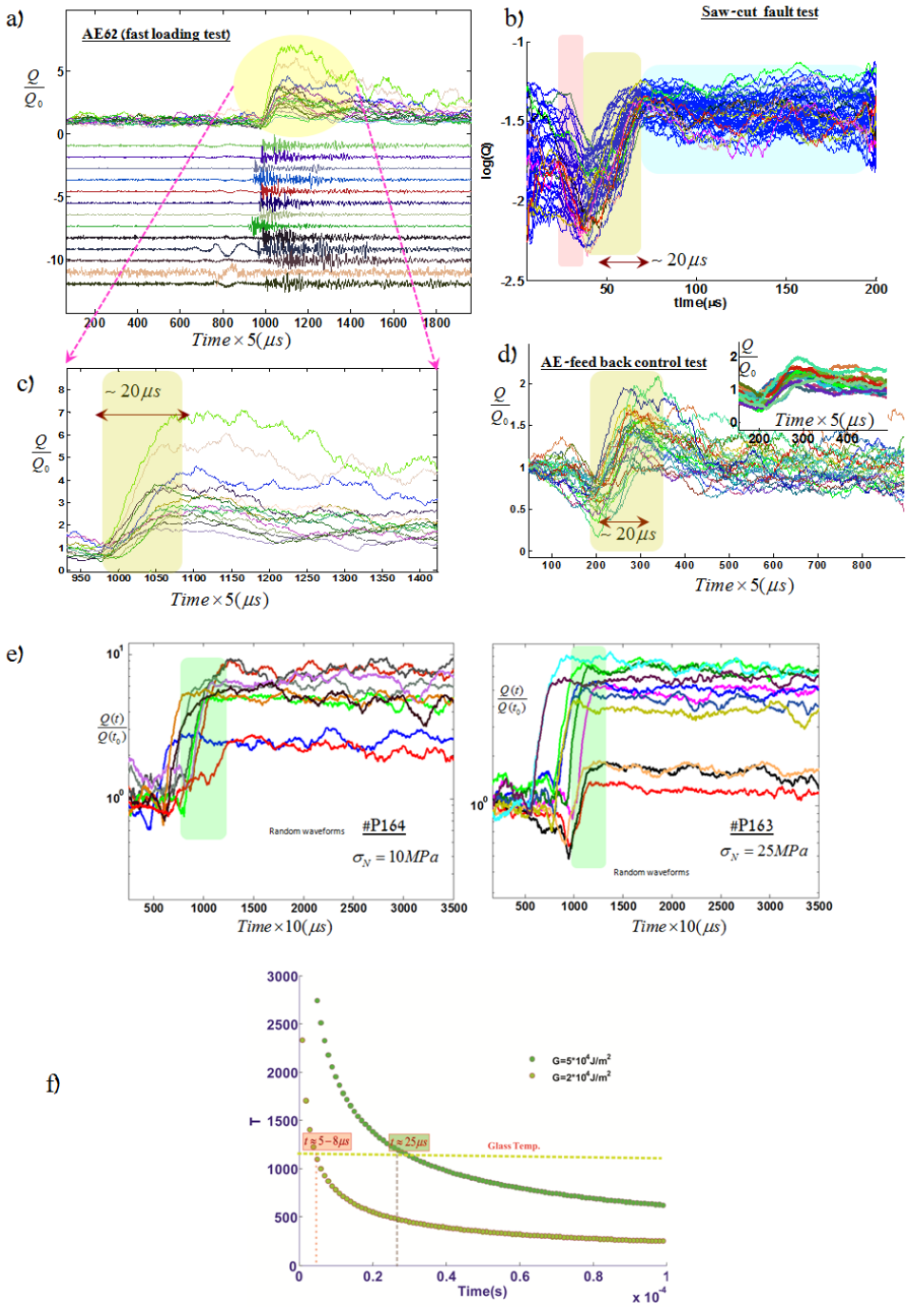

Figure S.2. (a-d) The loading condition and the geometry of the rock samples do not change the duration of the fast-slip phase in compressive triaxial tests. We have shown the normalized Q-profiles from different tests on Westerly Granite. (e) Q—profiles from a double-shear test with Quartz-sands as the gouge materials. (f) an effective temperature model on silicate(SiO_2) for two different fracture energies. Also see Fig.S.3.

In Fig.S.2, events from different stages of the fast-loading test (with strain rate $10^{-5}/s$ - Fig.S.2 a and c) are compared with events from saw-cut events (Fig.S.2b) and AE-feedback control tests (FigS.2d-see (4) for the details of the test and Fig.S1.f for the final cracks' configurations and AEs- sensors set-up)). In Fig..S.2.e, the Q-profiles have been shown from the events of the double shear experiment on gouge materials with quartz-sandstone (see the details of the experiment in Ref.5). As we have demonstrated, the second phase shows nearly a constant duration of ~20-25μs. Then, *the shorter fast slip phase in the TTT experiment <u>is not</u> due to the geometry, loading rate, nor other conventional loading conditions of samples*. This generic phase (and other phases extensively discussed in (6-7)) occurs due to the released energy from the failure or fast-deformation of an asperity or heterogeneity and is directly related to the physics of energy dissipation in vicinity of crack tip. In section 5 and discussion section of this document, we will show that unconventional micro crack nucleation shares an important common feature with anti-cracks as an extreme oblique cracks to the maximum stress field.

We also present experimental evidence that materials with significant ductility increase the duration of the weakening time. This non-linear character is well encoded in acoustic waveforms (excitations) and reflects the details of the physics of energy dissipation in the vicinity of the crack tip (Fig.S.3-aslo see section 2). For instance, micro-quakes in thermally treated Westerly granite (CTT test) and in room-temperature Westerly granite do differ about factor 1.7-2 in terms of duration of fast-slip time. At a fundamental molecular and atomic scale, we can assign this phenomenon to the growth of tiny voids and nano-cracks ahead of the potential micro-cracks; this will add more dissipative sources rather than creating just two crack surfaces. This is equal to the change in facture surface energy and increasing the duration of weakening phase. The result from the treated Westerly granite, in analogy to the crushed zone around the fault's core, does have a significant implication in natural earthquakes. This also implies that the rupture velocity is about two times slower (for the same shear stress drop). Considering the evolution of polymeric materials such as Polytetrafluoroethylene (PTFE) and PMMA [6], we infer that the weakening phases indeed are much longer. The question might be considered as follows: can we recognize the transition from elastic to plastic behavior in this fast strain/stress drop time? In fact, we could separate theses two distinguished phases with enough resolution (we will address these results elsewhere).

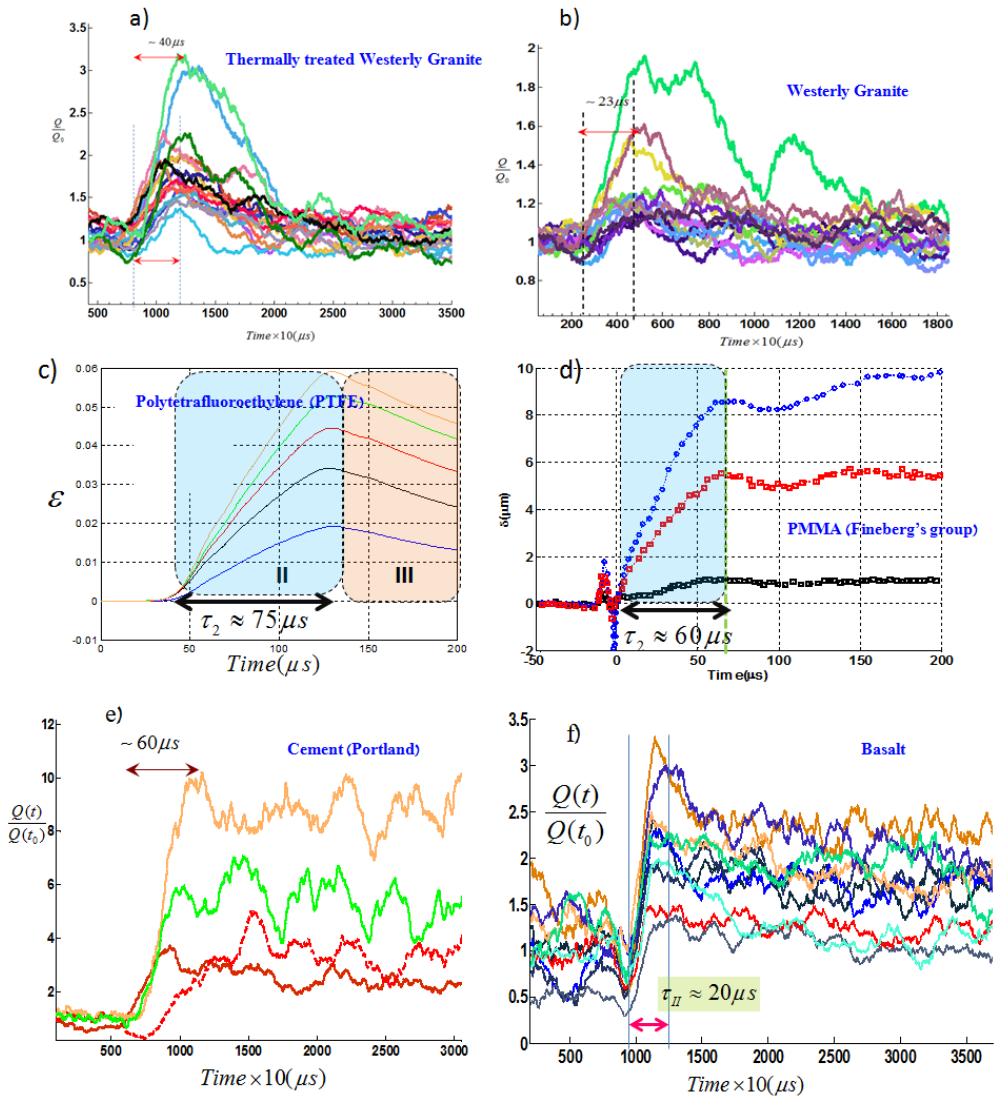

Figure S.3. Q-profiles from different materials and **signature of plasticity**. (a) normalized Q-profiles for thermally treated Westerly granite by 850 ^{o}C shows a longer weakening time (~35-40 μs) in micro-quakes while the same granite at room temperature reflects typical ~20μs weakening time-under CTT (b). This is due to the growth of inter-grain cracks (and other structural changes in quartz) which induce plasticity and add additional sources of energy dissipation rather than creating new surfaces . Thus, **induced nanoscale heterogeneities promote energy dissipation** (c) For Polytetrafluoroethylene (PTFE), the weakening time is longer ~75 μs similar to PMMA (d) as reported extensively in [6]. These results strongly indicate that adding dissipative energy sources stretch the duration of weakening time (i.e., smaller weakening rate) and for the same stress drop results in a smaller rupture velocity. As another application of analysis of micro-ruptures, we infer that any plastic deformation will be encoded in the weakening time with signature of softening in part of this period. If a material shows a negative weakening rate ,it is in a meta-material regime. For a shorter weakening time in TTT, we reach desired rupture velocity ~2-3 times faster. For ruptures with steep oblique propagation, reaching super-ruptures is easier (we can call them super anti-cracks).

(e) Q-profiles from concrete samples (cemented based materials- Courtesy of original waveforms : Dr. Katsaga ; Int. Journal of Fracture 148.1 (2007): 29-45.) show a longer period of the second phase indicating a higher toughness and additional energy dissipation mechanisms. (f) A dry basalt sample [data from Dr.P.Benson-(9)] reflects ~20micro-seconds duration of fast-slip phase, very close to room temperature granites and sandstones in CTTs.

-<u>On Mechanical Interpretation of Functional-Acoustic Networks</u>

In this part of the study, we show that (1) modularity profiles are reminiscent of dynamic stress changes per each event ; (2) $\overline{\lambda}_{\max} - \overline{\log < B.C >}^{-1}$ parameter space can be used to infer weakening rate and then rupture velocity in the scale of micro-ruptures and (3) slip tendency patterns can be inferred from multiplex networks using $\overline{\lambda}^{x,y,z}_{\max} - \overline{\log < B.C >}^{-1}_{x,y,z}$.

As we have shown in Fig.2.(main text), the main time characteristics of the evolutionary phases of Q-profiles and their trends from micro cracks coincides with dynamic stress change profiles in macro-ruptures (a few centimeter scale) . Then, we infer that the maximum Q (t) corresponds with the maximum stress drop ($\sigma_{\min.}$) in micro and sub-micron cracks. The initial drop of the Q-profile (as the nucleation and strengthening phase) before the weakening phase corresponds with maximum strength of heterogeneity (or asperity). The minimum value of Q (or maximum value of R) coincides with $\sigma_{\max.}$ Inferring this $\sigma_{\max.}$ in each main direction (such as X-Y-Z) will provide the ingredients to infer local failure criterion. For this reason, we address maximum values of R in three main directions in our TTTs.

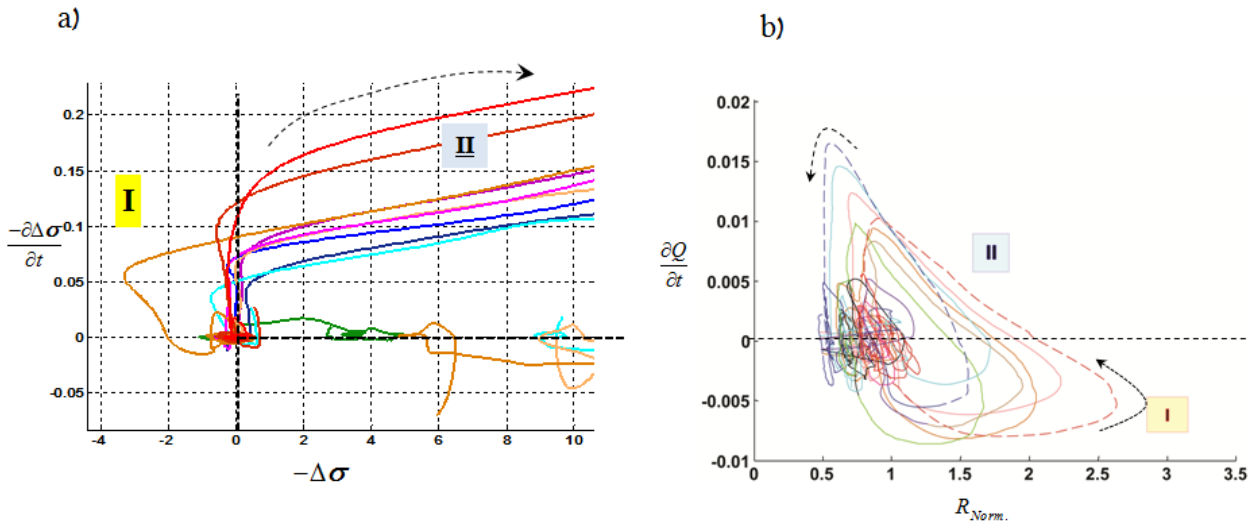

Figure S.4. Dynamic stress rate versus stress change in CTTs .We have distinguished two successive phases as the initial strengthening (I) and weakening phase (II) for the macro-ruptures . (a) The details of the first phase and (b) rate of modularity index versus normalized R-values for micro-events (from Saw-cut fault experiment on Westerly Granite [18]). Maximum R(t) is considered as the peak of strength, just before the onset of fast slip phase.

Another feature regarding studies of Q-profiles is the rate of the second phase or the weakening rate. Increasing the weakening rate corresponds with increasing rupture velocity. Then, classification of weakening rate likely provides information on statics of rupture velocity. We have addressed this issue in our recent study in [7]. How about temporal-mean of Q-profiles ($\overline{Q}$) ? To answer this question, we address the skewness of Q-profiles as the metric to characterize symmetry in signals. Generally, signals with a high weakening rate imprint high left-asymmetric shape .In addition, increasing $\overline{Q}$ decreases skewness (Fig.S15b). As a result, increasing $\overline{Q}$ corresponds with smaller weakening rate (and slower rupture). We also note that $\overline{Q} \propto \frac{1}{\overline{\lambda}_{\max.}}$. This will complete our interpretation of $\overline{\lambda}_{\max} - \overline{\log < B.C >}^{-1}$ plane. Events with higher $\overline{\lambda}_{\max}$ indicates ruptures with higher asymmetric shape likely with high rupture velocity. However, increasing the duration of fast slip phase (resulting slower weakening rate and then slower rupture velocity) leads to smaller $\overline{\lambda}_{\max}$ (and higher $\overline{Q}$) . This possibly form a new separated cluster in $\overline{\lambda}_{\max} - \overline{\log < B.C >}^{-1}$ corresponding to slower ruptures or creep events

equivalent with plastic deformation (in a crack tip or generally a hyper-elastic zone). In fact, during crackling, part of the energy stored in the crack tip is transformed into breaking molecular (and atomic) bonds/contact areas, resulting in new surface(s) of cracks (i.e., fracture energy). The *quality* of the aforementioned failures dictates the rupture regime where a non-linear zone is formed in vicinity of the rupture tip.

Let us conclude: First of all (1) $\overline{Q} \propto \frac{1}{\overline{\lambda_{\max.}}}$. and (2) $\sigma^{-1}(t) \propto Q(t)$ and then $R(t) \propto \sigma(t)$. Let's assume two different rupture fronts with two unequal weakening rates: $\dot{\gamma}_1 < \dot{\gamma}_2$ and $\overline{R_1} < \overline{R_2}$ (bar sign is the temporal mean over a fixed mentoring time such as 300 micro-seconds). Then, $\overline{Q_1} > \overline{Q_2}$ and from (1) we reach to : $\overline{\lambda_{\max.(1)}} < \overline{\lambda_{\max.(2)}}$. The higher weakening rate holds higher $\overline{\lambda_{\max.}}$. On the other hand, a higher weakening rate indicates higher rupture velocity. Thus, $\dot{Q}_{II}^{(1)} < \dot{Q}_{II}^{(2)}$ which shows the rate of the second phase in Q(t). For this reason, ruptures with higher velocity and energy allocate the *right-hand tail* of $\overline{\lambda}_{\max} - \overline{\log < B.C >}^{-1}$ parameter space.

Regarding interpretation of $\overline{\log < B.C >}^{-1}$,we note that minimum value of $\log < B.C >$ is generally coincided with the large amplitudes of waveforms (Fig.S.5). Then, we infer rupture with high energy will have larger $\overline{\log < B.C >}^{-1}$. The second derivation of Q(t) approximately matches with $\frac{1}{\log < B.C >}$ so that singularity is encoded in the inverse of centrality (See Fig.S.5) . Thus, the temporal curvature of Q(t) in the first and the second evolutionary phases is reflected in $\frac{1}{\log < B.C >}$. This indicates that sharper (temporal) curvature results higher $\overline{\log < B.C >}^{-1}$; In other words, dramatic sharp transition leads to fast-weakening rate (i.e., higher rupture velocity) . Let us focus on the first phase: the first phase is initial strengthening phase leading to maximum strength and failure point. Obviously, this initial strengthening phase shows the initiation of loading to the final stage and thus includes loading details . Transition in curvature of loading path (stress-time or stress-strain) results stiffening or softening mechanism . We can assume that this signatures are closely related to hyper-elastic (or non-linear elastic) region

around the crack tip . With this connection, we now refer to atomistic modeling of crack propagation with considering the effect of stiffening (or softening) in loading stage (for instance see Fig.4b in http://www.nature.com/nature/journal/v439/n7074/full/nature04408.html) . The molecular dynamic models show that sharper transition leads to faster crack instability speed . Indeed, our results confirms these simulations results: drastic transition in curvature results a big amount of decrease of $\log < B.C >$ at the critical point ,which result high amount of $\overline{\log < B.C >}^{-1}$. Also, empirically, we showed that $\overline{\log < B.C >}^{-1}$ scales with weakening rate so that higher weakening rate increases rupture velocity . Then, drastic transition in curvature of Q in the first and second stage is reflected in crack instability speed .

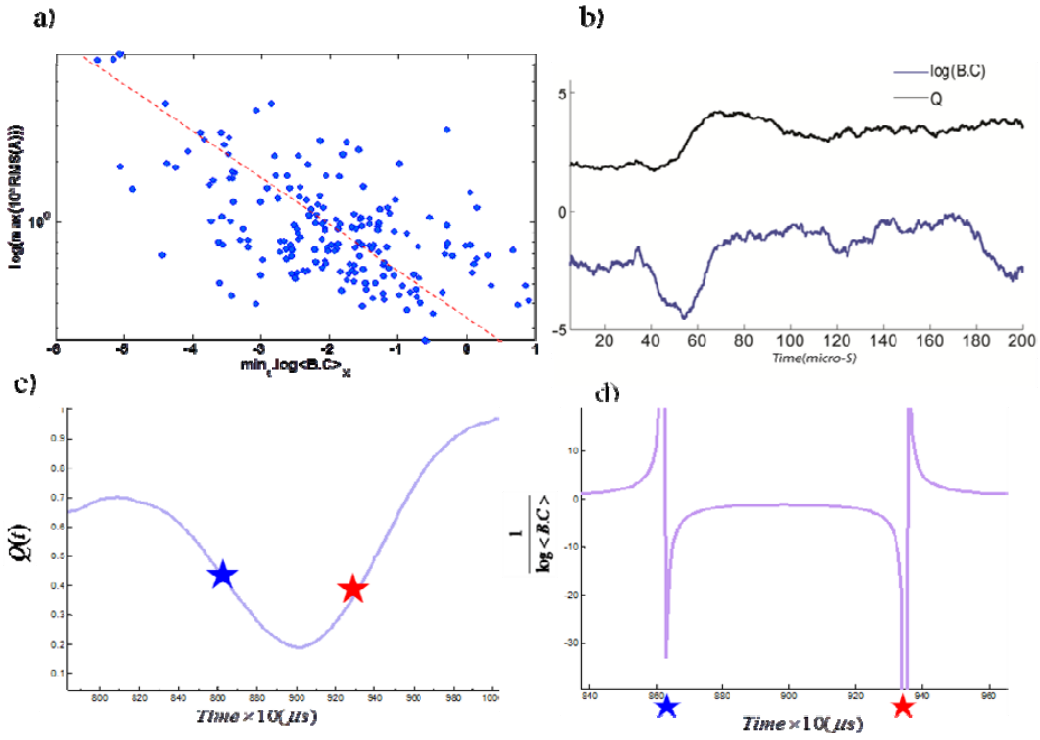

Figure S5. Minimum value of mean centrality generally scales –inversely- with maximum amplitude of waveforms(a) . Two typical signals of modularity and centrality profiles from CTT (b). In panels (c) and (d) ,we compare Q(t) and the corresponding temporal variation of $\frac{1}{\log < B.C >}$,respectively. The second derivation of Q(t) approximately matches with $\frac{1}{\log < B.C >}$ so that singularity is encoded in the inverse of centrality . Thus, the curvature of Q(t) in the first and the second evolutionary phases is reflected in $\frac{1}{\log < B.C >}$. This indicates that sharper (temporal) curvature results higher $\overline{\log < B.C >}^{-1}$; In other words, dramatic sharp transition leads to fast-weakening rate .

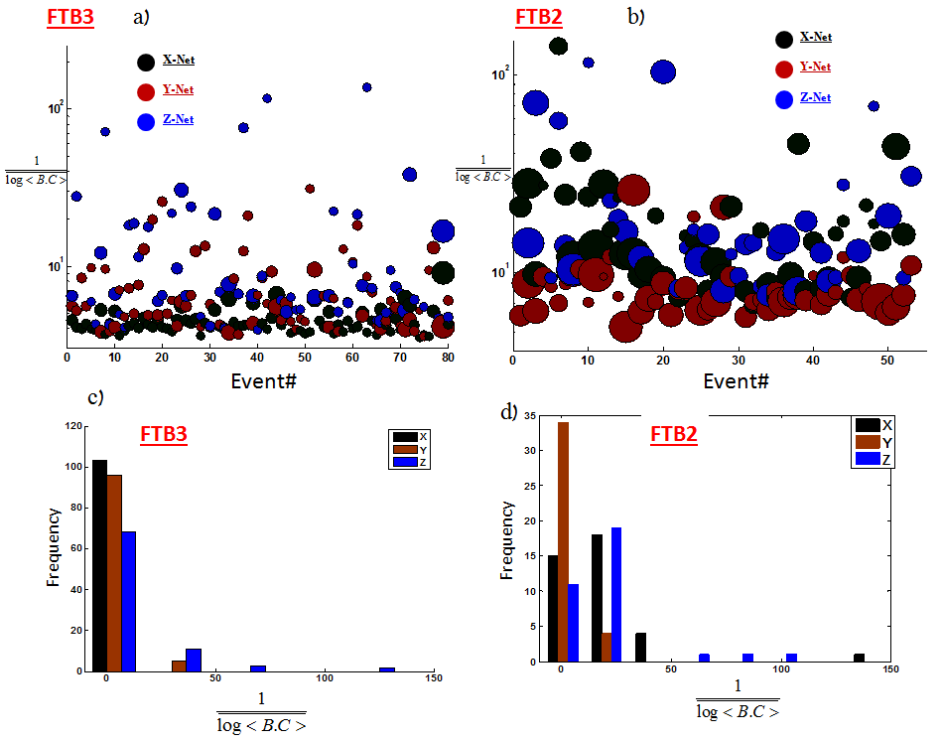

Figure S 6. The activity of three layers of multiplex networks for FTB3 (a) and FTB2(b). The most high energy events in FTB3 reflect in Y-Z layer(c) while in FTB2, X-Z layers are prevalent (d). See also section 3 for more results on multiplex networks

In further analysis of Q-profiles and R-profiles (the methods part in the main text), in Fig.S.7 , we have compared the R-profiles from TTT and CTT while the details of the evolution of a typical R-profile are shown in Fig.S.4c. The onset of the deformation proceeds with the fast rise in a very short time (~2-6μs) to reach maximum R(t). We choose this maximum R-value from three sub-networks (corresponding to three main Cartesian directions in cubic-samples), when we are analyzing the sub-networks' metrics. The fast decrease (drop) of R profiles corresponds with the fast-slip phase of Q-profiles; then is longer in CTT 's events.

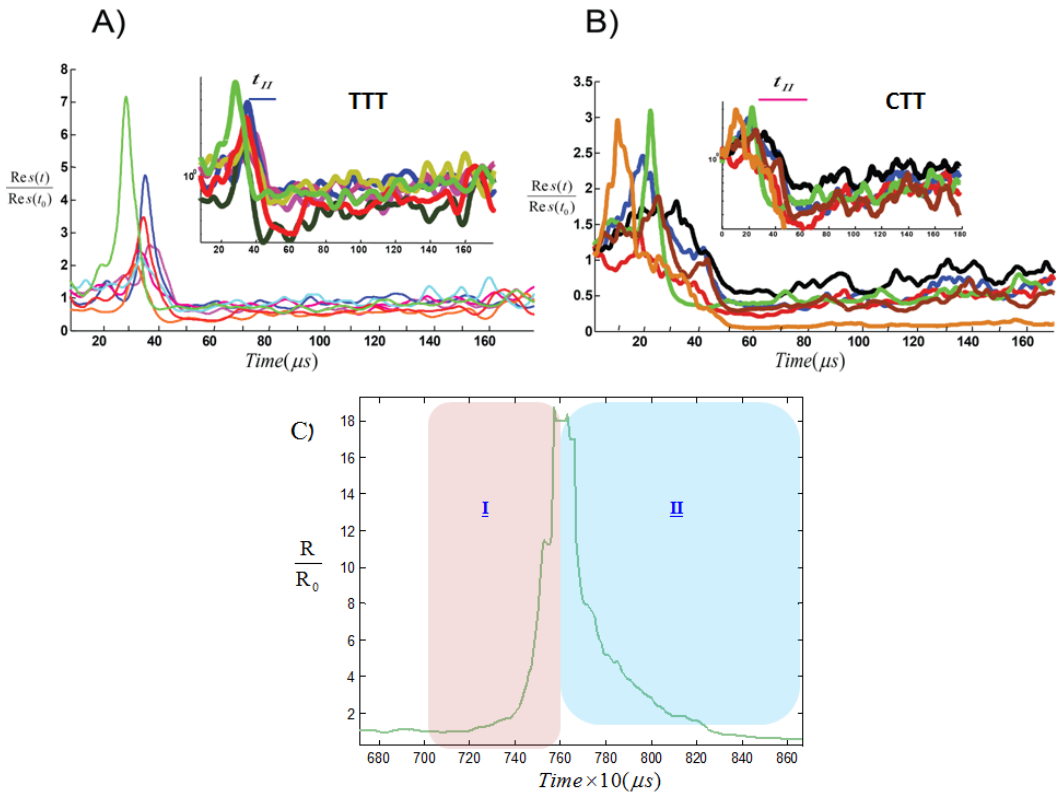

Figure S.7. (a,b) Examples of R-profiles from the TTT (FTB4) and the CTT. Inset: semi-logarithmic R-profiles. **(c)** a typical R-profile includes two main sub-phases: (I) onset of nucleation and fast-rise (~4-8μs) leading to the maximum R (initial strengthening phase) and (II) fast-slip part as the weakening phase is imprinted as the fast-decay section of R-profile. As it can be inferred from the comparison of panel(a) and (b) ,the duration of this phase is longer for CTT.

The evolution of R-profiles (or Q-profiles) in terms of approaching the rest state (in normalized form to 1), is faster in TTT than CTT, indicating that the healing mechanism for this kind of stress regimes is probably faster . The reason can be inferred from the possible correlation of the last evolutionary (dynamic) phase of the Q-profiles with the growth of contact areas as has been shown in (6). Then, not only is the fast-slip phase shorter, the slow-slip is shorter and the onset of healing occurs earlier than in other, simpler tests.

Next, we visualize the spatio-temporal average of the global network's metrics (Fig.S.8c-also see (7)).For each best located event, we calculate $\frac{1}{\log < B.C >}$ and $\overline{Q}$. Considering that the large amount of $\frac{1}{\log < B.C >}$ corresponds with high-energy tiny ruptures, we conclude that the

internal patches of the Orthorhombic fault-system release higher energy than the external patches. The results do match the $\overline{\lambda}_{\max}$ -$\overline{Q}$ phase diagram of global networks (Fig.S.5a-b). The global network parameter spaces –as have been mentioned in the main text- show a significant difference of trend in comparison with the CTT (or events from the rough frictional interfaces).

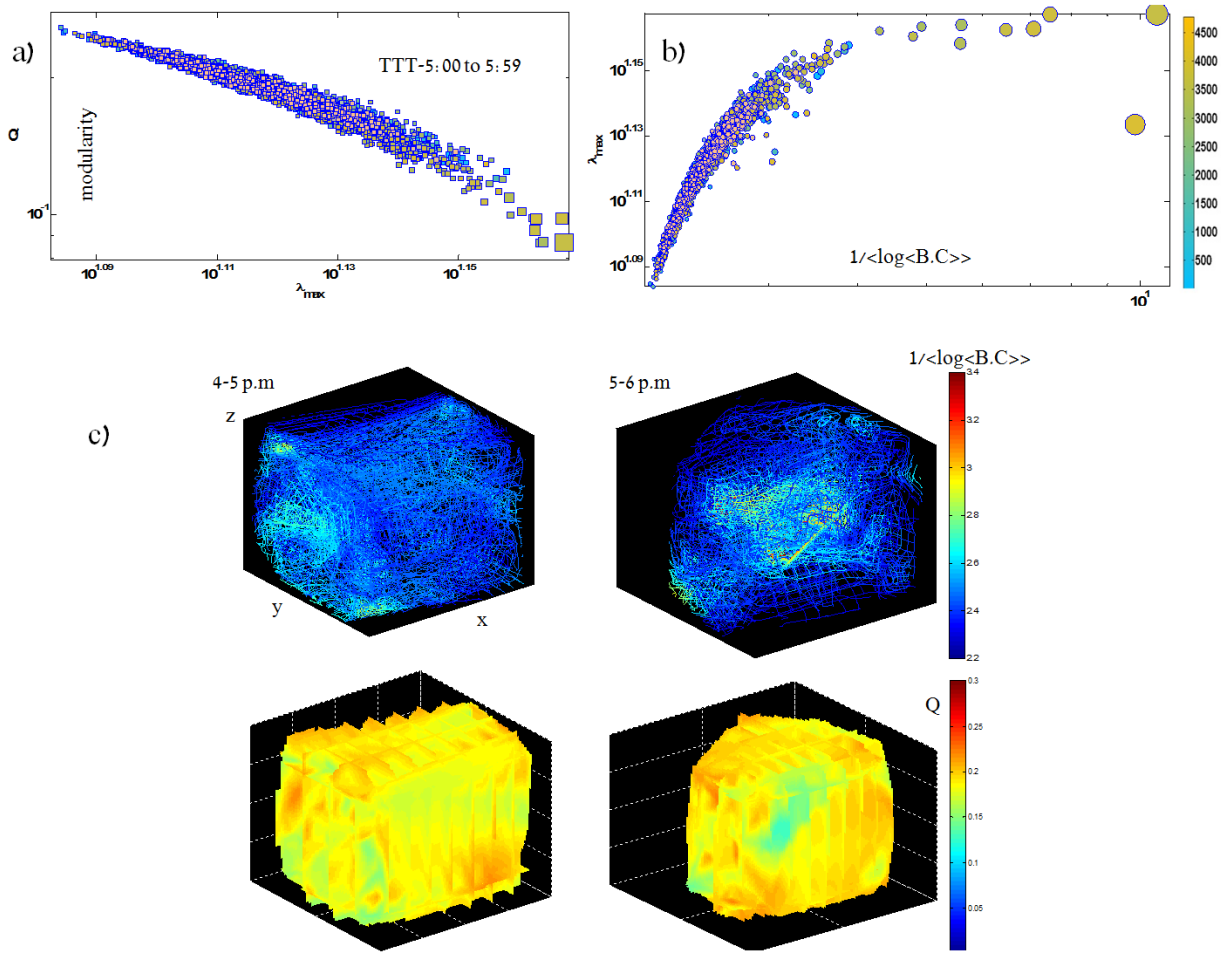

Figure S.8 Spatial distribution of the temporal average ensemble of network parameters (global network attributes) . (a-b) Global network phase spaces on all detected events (~4500 rupture fronts) in the hour leading to the main stress drop. The size of the circles is proportional with the maximum of $\frac{1}{\log < B.C >}$. Generally, events with higher energy allocate larger and smaller values of $\frac{1}{\log < B.C >}$ and $\overline{Q}$, respectively. (c) **The top-panel** shows the $\frac{1}{\log < B.C >}$ during the two hours of the experiment (visualized by 3D contour lines). Dense activity and high-energy events are formed in the second hour of the experiment while the main failure (and internal patches of M-shape fault system) occurs. **Bottom panel**:

Distribution of $\overline{Q}$ in the second hour of the experiment. This can be assumed as an indicator of brittle or ductile deformation in micro-scales (since $\overline{Q} \propto \frac{1}{\lambda_{\max.}}$).

2. Calculation on the fast-slip phase of Q- profiles

The model to be used here is a polycrystalline material subject to a simple shear stress. Our key assumption is that generally the motion of a sub-micron crack is governed totally by a thermally activated depinning mechanism. Similar to (6), we propose an effective temperature to explain the observed time scales. As another approximation, because over 90% of Fontainebleau sandstone is quartz minerals, we solve the equation for silicon dioxide on the scale of sub-microns. We also use an approach suggested for the left-hand asymmetric shape of the (average) of avalanches in crackling noise systems (ruptures induced acoustic emissions and Barkhausen noise). Based on this approach (11-12), the asymmetric average shape of the avalanches is due to the role of energy dissipation phenomena (eddy currents and strengthening threshold). Here, we use an equal version for energy dissipation phenomena, originally proposed in (6) and (7) to explain the sudden drop of one of the evolutionary phases (i.e., the onset of the phase III in Fig.S.2.b). A fast-short time fracturing (phase I) induces a very fast increasing the temperature of a tiny "process zone" which is becoming cooled down in a typical time characteristics. The main component of the theory is that the fracture energy is encoded in terms of the diffusion of heat. The increased temperature with respect to a reference temperature is as follows (6):

$$\Delta T = \frac{-G_t}{4\rho c_p h}\left[erf\left(\frac{-h}{\sqrt{4D_T t}}\right) - erf\left(\frac{h}{\sqrt{4D_T t}}\right)\right] \qquad \text{(S1)}$$

in which h is the thickness of the process zone in which the energy rapidly dissipates, D_T is the thermal diffusivity , G_t is the fracture energy , and t is the cooling time . With first-order approximation, we estimate t as follows:

$$t \approx \frac{G_t^2}{\Theta}, \Theta = 4(\Delta T \rho c_\rho)^2 \pi D_T \qquad \text{(S2)}$$

in which Θ is a constant value for a given material. We assume $t \approx t_{II}$.

To proceed further, we plot the variation of effective temperatures for different fracture energies for SiO_2 in Fig.S.2f. From Fig.S.2.f we have : $t_{II}^{CTT} \approx 20-25\mu s$ and $t_{II}^{TTT} \approx 8-10\mu s$ (For TTT-

see also section 4), which results in $G^t_{TTT} / G^t_{CTT} \approx .4 - .6$. We note that increasing the rate of fast-slip (shorter *t*) phase corresponds with the smaller encoded energy at the second phase. Our results prove that (under normal conditions) increasing toughness is encoded in the duration of the second phase. When considering the invariant nature of the second phase under different confinement loadings in CTTs (and other simple tests), we infer that shorter generic stages for the same materials are due to different substantial nature of cracking in micro/sub-micron-scales (and sources of energy dissipations). Since the reported phase –also-is observed in different stages of the test (while source mechanism changes), then we cannot link to the source mechanism (obtained from P-wave arrival). Interestingly, we find out that the second time interval is longer for concrete –as the cement based materials-due to the cement component and Calcium-Silicate-Hydrate (C-S-H) structures (Fig.S.3). This is due to additional sources of energy dissipation rather than just creating new surfaces (Buehler&Keten-Rev.Mod.Phys 2010). Also we find out this phase is about ~70μs for TEFLON (as a polymer-amorphous material), close to ~60μs for PMMA (6). Then, tougher materials –with additional energy dissipation sources in a crack tip-imprint a longer fast-slip or weakening time phase, which proves the aforementioned approximation. With canceling or suppressing the sources of energy dissipation, we reach the shorter phase, meaning much faster-release energy. We believe that in our TTTs, this phenomenon does occur, coinciding with the sort of anti-cracking propagation in mesoscale. In fact, anti-cracks are an extreme case of anisotropic cracks and then are closely related to study of slip-tendency (or friction anisotropy). Extending this approach, we can present a map of toughness (proportional to the duration of the second phase) versus strength per each event which resemble Ashby map of the damage tolerance. Indeed, we elucidated that adding dissipation mechanisms such as amorphization at the vicinity of crack tip, crack surface reconstruction (healing), lattice trapping or shuffling of lattices will alter this phase (Buehler&Keten-Rev.Mod.Phys 2010).

In section 4of this document, we find a link between the micro-cracks' activity in each layer and the duration of the second phase, supporting our approach to the irregularity of caking in some of our TTTs. This violates the conventional perspective on shallow earthquakes which assume earthquakes occur by ordinary fracturing developing in maximum and intermediate principle stress planes.

3. Studies on the functional Sub-Networks (independent layers)

In Fig.S.9, we have shown the procedure to establish sub-networks or layered layers (as a category of multiplex networks). Each direction (X,Y and Z) is an independent layer with N=6 nodes (extended to 18 nodes –see Methods section). We only consider the edges within the layers and the links between layers are not considered. Fig.S.9c shows an example of the R-profiles from each layer. Further study of each layer's network metrics indicates some interesting features in terms of the mechanical interpretation of rupture properties in that layer.

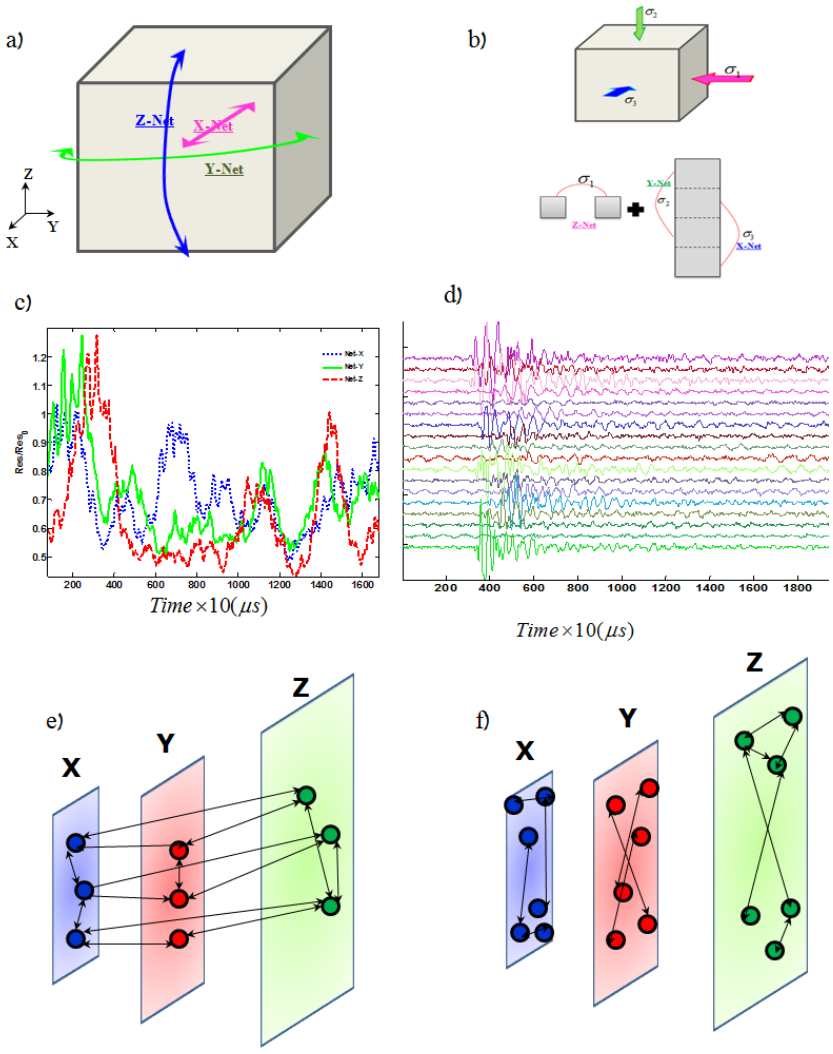

Figure S.9 (a-b) An illustration of sub-networks (or simply layers) in X, Y and Z directions; we use each layer of the network as an independent network. Parallel faces from a cubic sample form sub-networks of acoustic-sensors (or layer X, Y and Z) . (c) An example of R-profiles in each layer. (d) A typical recorded event through 18 transducers in ~180μs. Schematic of (e) global networks with 3 nodes in each layer and f) independent layers with 6 nodes in each layer.

In Fig.S.10 –S.11, we have shown the collapsing of the best-strong events (i.e., $\{R_i^l\}_{i=1,2,3} > 1$) in local network parameter spaces : $\frac{1}{\log < B.C >_{x,y,z}} - \overline{\lambda}_{\max_{x,y,z}}$. While the events are the identical events, Z-networks (σ_1 sensors) exhibit –on average- a long tail toward a high value of $\frac{1}{\log < B.C >}$. Hence, the X layer (σ_3 direction) holds slightly higher $\overline{\lambda}_{\max.}$ (also see Fig.S.6).

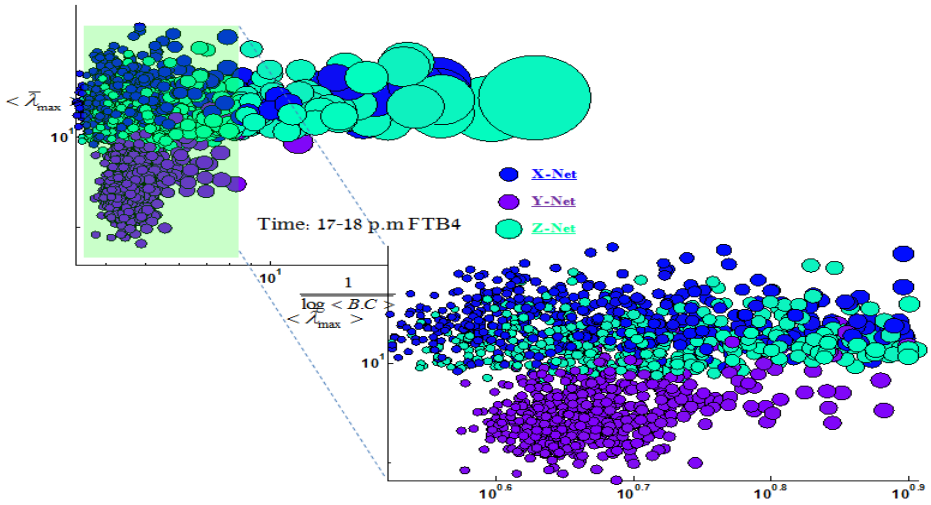

Figure S.10 $\overline{\lambda}_{\max.} - \overline{\log < B.C >}$ phase space for an hour of the FTB4 experiment. The size of the circles are proportional with the maximum of $\frac{1}{\log < B.C >}$. X and Z layers hold a high activity of the mapped events (corresponding to bigger $\frac{1}{\log < B.C >}$) with smoother trend in this phase diagram. Since events are not limited to a particular time or position, we interpret that the probability of growing micro-cracks in X-Z plane (minimum-max stress plane) is higher than other possibilities [also see Fig.S.6].

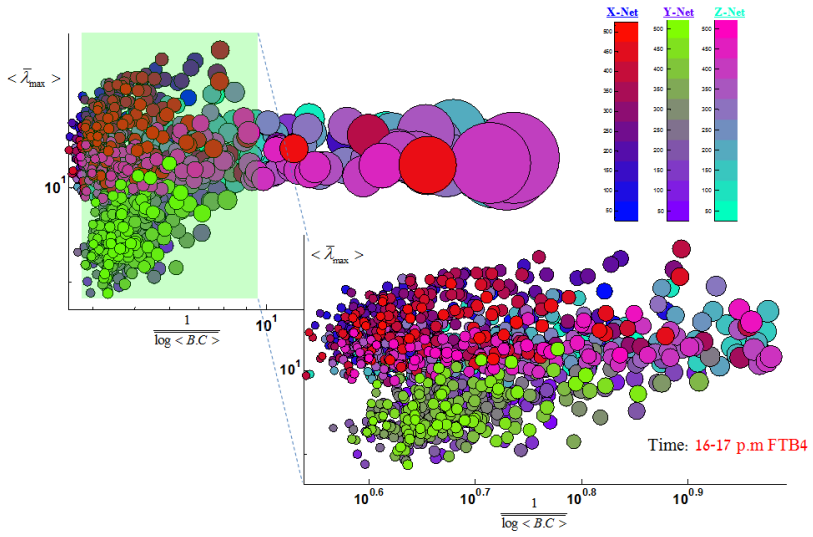

Figure S.11 $\overline{\lambda}_{\max.} - \overline{\log < B.C >}$ phase space for an hour of the FTB4 experiment. Considering a power law such as $\overline{\lambda}_{\max.} \sim \overline{\log < B.C >}^{-\chi_i}$,we have : $\chi_y \geq \chi_x > \chi_z$. The size of the circles is proportional to the maximum of $\frac{1}{\log < B.C >}$.

Moreover, events in the (R_1^I, R_2^I, R_3^I) parameter space do not show a clear relation while the totally diverse distribution in the aforementioned parameter spaces is collapsed in a universal power law when we use $J_1 = R_1^I + R_2^I + R_3^I$ and $J_2 = R_1^I R_2^I + R_2^I R_3^I + R_1^I R_3^I$ (Fig.S12-S.13-S14). As we indicated, the maximum value of R-profile (at the onset of the fast-slip regime) is interpreted as an indicator to the maximum dynamic strength in sub-micron rupture scale. Then, maximum R values in each layer are assumed as a principle component of deformation's attributes. With this interpretation, we used a similar definition to the first and second invariants ($J_1 = R_1^I + R_2^I + R_3^I$ and $J_2 = R_1^I R_2^I + R_2^I R_3^I + R_1^I R_3^I$) to speculate about possible failure criterion in micro-cracks. This procedure reveals a very close power law coefficient to previously reported similar criterion by Reches (3) on different rock-samples.

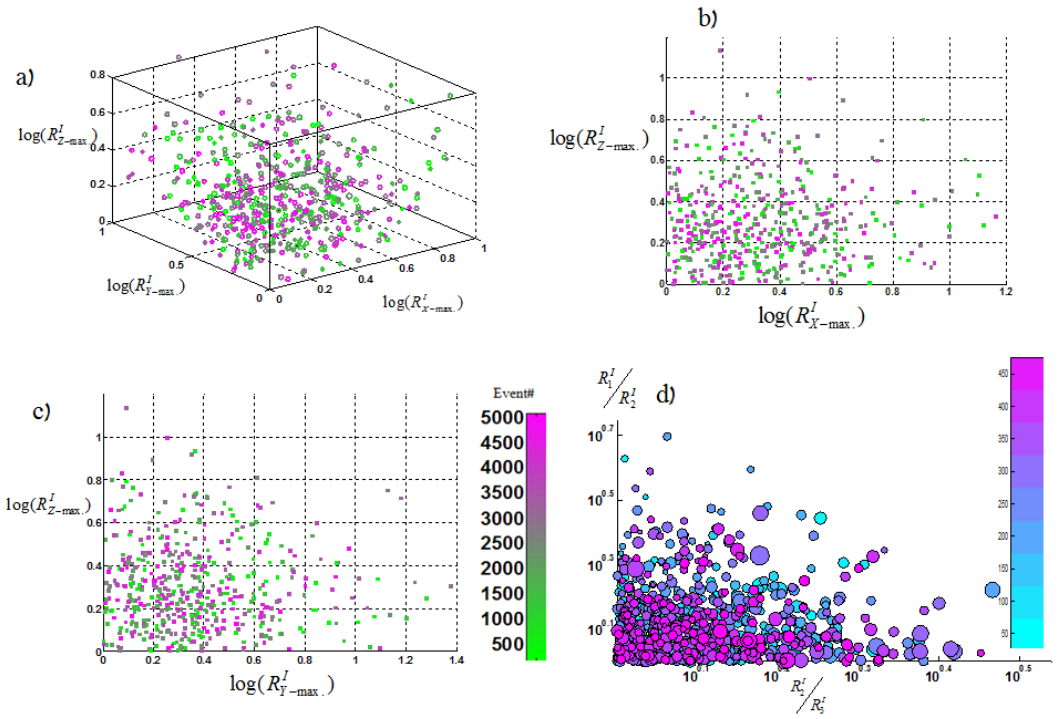

Figure S.12 Precursor events in **the** $(R^I_{x-\max}, R^I_{y-\max}, R^I_{z-\max})$ parameter space do not show a clear relation between the maximum resistivity (or strength) of the events in the main directions. However, interestingly, the totally diverse distributions in the aforementioned phase spaces are collapsed in a universal power law while we use $J_1 = R_1^I + R_2^I + R_3^I$ and $J_2 = R_1^I R_2^I + R_2^I R_3^I + R_1^I R_3^I$.

Likewise, in Fig.S.13 (a and c) and Fig.S.14a, indentifying a similar parameter to octahedral shear stress $\Upsilon_R = \sqrt{(R_1^I - R_2^I)^2 + (R_2^I - R_3^I)^2 + (R_3^I - R_1^I)^2}$, we could obtain the parameter spaces shown in Mogi (13) and Haimson (14). Now, with the interpretation of $\log \Upsilon_R \propto \beta \log R_1^I$ (Fig.S.13e, Fig.S.14a) as the local failure characteristics and considering $\log \Upsilon_R \propto \tau_{oct}, \log R_1^I \propto \sigma_{\max}$, we reach the similar -Coulomb law**:** $\tau \propto \beta\sigma$ (also see last section for analysis of simpler tests 'events from saw-cut and rough fault of Westerly Granite rock samples).

The skewness (Eq.3-Methods part) of Q-profiles (of global network) is positive, showing a left-hand asymmetric shape of the pulses. Ruptures with higher energy (smaller $\overline{Q}$**)** hold a relatively more asymmetric shape (Fig.S.15). With approximation, an asymptotic curve may be fitted on global skewness (Σ_g)-J_2phase space, indicating that the larger J_2 or J_1 leads to an average (or medium) skewness of Q-profiles (Fig.S.15d). Considering that largerJ_1possibly results in longer waveforms and the relation among pulse duration and skewness in crackling noise systems (see Fig 28 in (15)), we conjecture that the results are similar to the aforesaid figure: longer waveforms approach smaller leftward asymmetry.

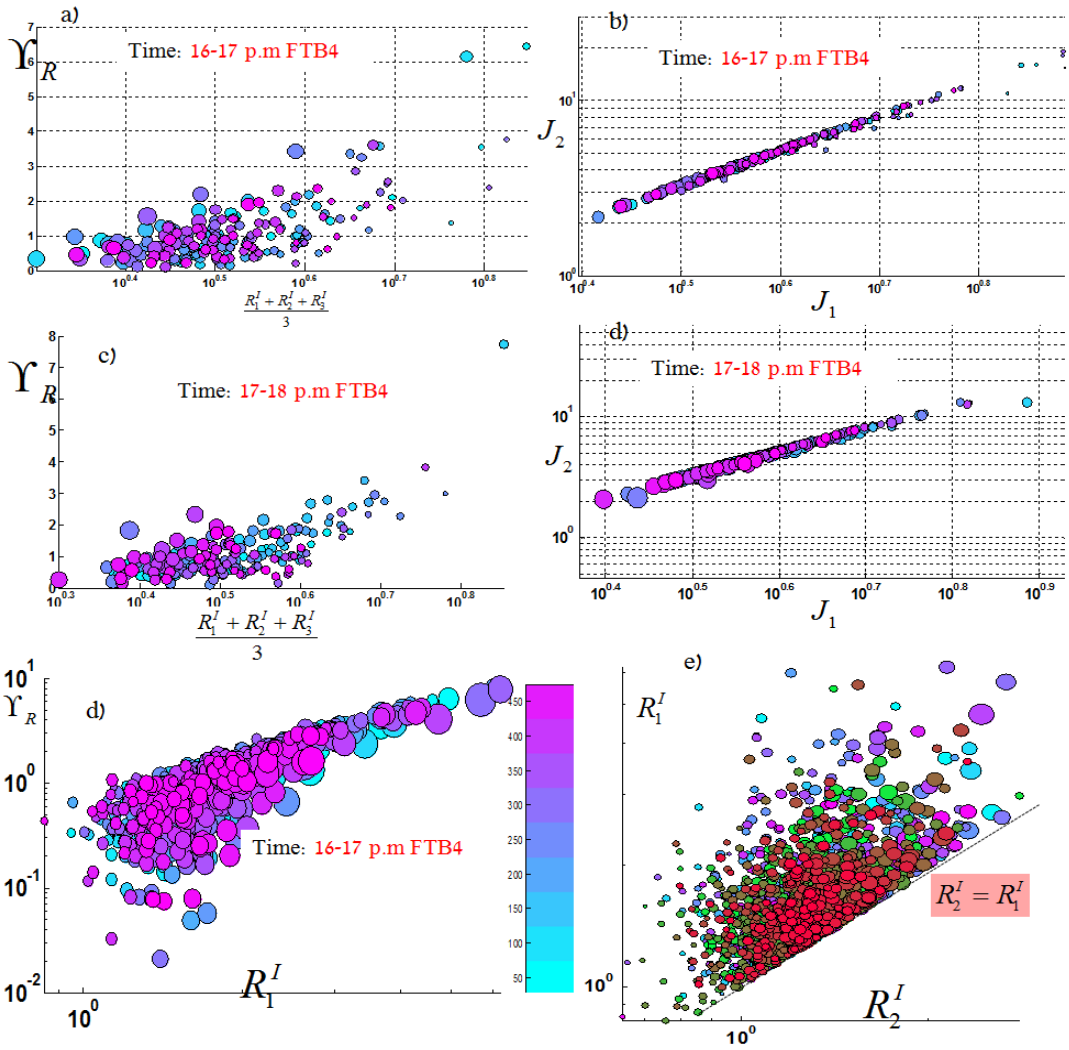

Figure S.13 Failure criterion with minimum modularity of sub-networks . (a,c) Collapsing ~520 best-strong events from the FTB4 tests in Υ_R - $R_1 + R_2 + R_3 / 3$ parameter space from two hours of the experiment, where $\Upsilon_R = \sqrt{(R_1^I - R_2^I)^2 + (R_2^I - R_3^I)^2 + (R_3^I - R_1^I)^2}$ (similar to octahedral shear stress-also see Ref.(3) and Ref.(13-14) for the similar scaling over final failures). (b,d) Phase diagrams in $J_1 = R_1^I + R_2^I + R_3^I$ and $J_2 = R_1^I R_2^I + R_2^I R_3^I + R_1^I R_3^I$. A power law function satisfies an excellent collapsing of events in the J_1-J_2 phase diagram as: $J_2 \propto J_1^b, b \approx 2.6$. (e) Υ_R-R_1^I (with $\Upsilon_R \propto R_1^\beta$) shows that most of the events are collapsed in an interval with one order of magnitude difference on the Υ_R axis. This trend slightly changes after a threshold level of R_1 (on average, decreasing β), comparable with panels a and c. The size of circles in a-e are proportional to the R_2^I. (f) $R_2^I - R_1^I$ plane for two successive hours of the experiment. The size of circles is proportional to R_3^I. See also section 5 for more analysis of the parameter spaces in the simpler experiments.

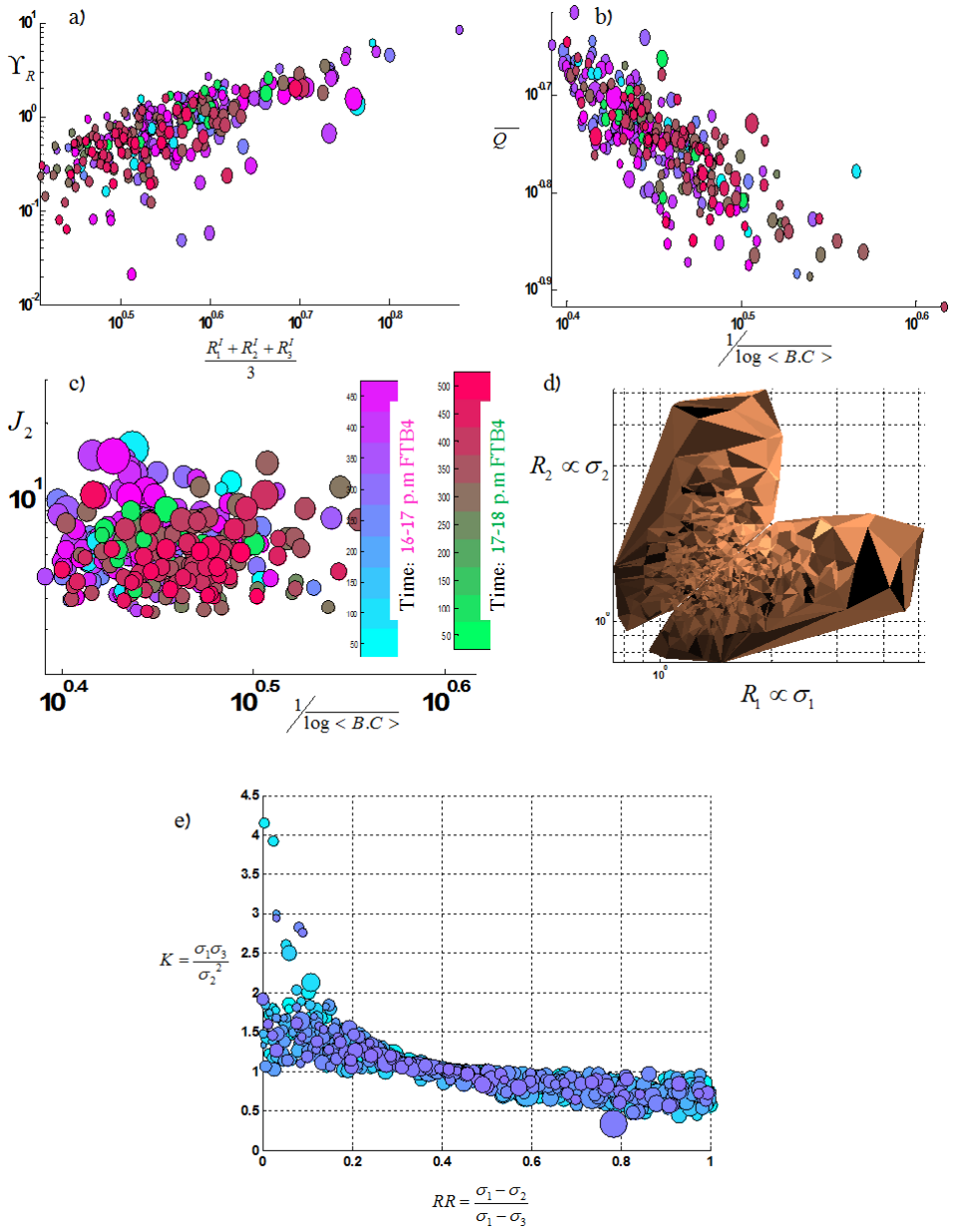

Figure S.14. Studies of network phase spaces. We have shown the events from two hours of the experiment (before main stress drop) in local (a) global (b) and global-local phase diagrams. The size of the circles are proportional with the R_2^I in that occurred event. While (a) and (b) confirm the scaling of attributes, (c) does not show such a correlation. The size of the circles is proportional to to R_2^I. (d) We have shown a collection of planes on the triple points of max-R values for events that occurred ~an hour before the final failure (i.e., locus of local-yield surfaces). E) Stress fields where K=1 have bimodal distributions of surfaces with high slip tendencies . When K>1, the distribution of high slip tendency surfaces tends toward σ_1 and for K<1 tends toward σ_3 (*Morris, A., Ferrill, D. A., & Henderson, D. B. (1996). Slip-tendency analysis and fault reactivation. Geology, 24(3), 275-278.*).

Relation between Global and Sub-Networks (independent layers)- Next, using the simplified scaling relations, we infer the possible relation of fracture energy (inducing the duration of the second phase in Q-profiles) and local sub-networks (i.e., sub-micron/micron or precursor fronts' failure criterion). To proceed, the upper bound of the $J_2 - \Sigma_g$ phase diagram is approximated with $J_2 = \exp(-(\Sigma_g - \Sigma^c_g))$ and then replacing with $\Sigma_g \propto \overline{Q}^{-l}$, It leads to $J_2 \propto \exp(-\overline{Q}^{-l})$ for the upper bound (or approaching from the top). We further assume that the power-law coefficient l is identical for both TTT and CTT. In addition, due to shorter generic phases of TTT (while we average over the same time interval), we expect $\overline{Q}_{CTT} > \overline{Q}_{TTT}$ which yields $J_2^{CTT} > J_2^{TTT}$ for $\Sigma_g > \Sigma^c_g$ (and vice versa). We conclude that higher than a threshold level, higher J_1 (or J_2) couples with a higher fracture energy then resulting in a slightly lower β in $\Upsilon_R \propto R_1^{\beta}$. Then, we connected global networks to local sub-networks' metrics.

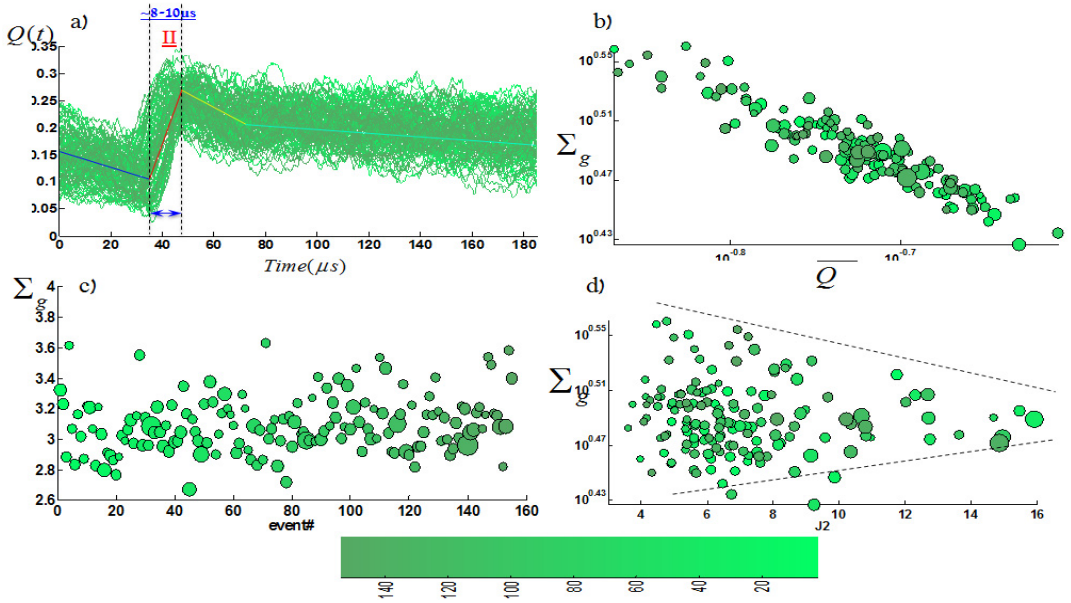

Figure S.15. The average skewness of Q-profiles from global networks. (a)A collection of ~160 events in TTT (FTB4), schematically representative of generic phases of Q-profiles. (b) $\Sigma_g \propto \overline{Q}^{-l}$: skewness versus mean modularity .(c) The evolution of skewness for the sequence of events. (d) Global skewness versus local metric of maximum R values from sub-networks. The dashed lines show the upper and lower bounds/trends of events. The size of circles is proportional to to R_2^I.

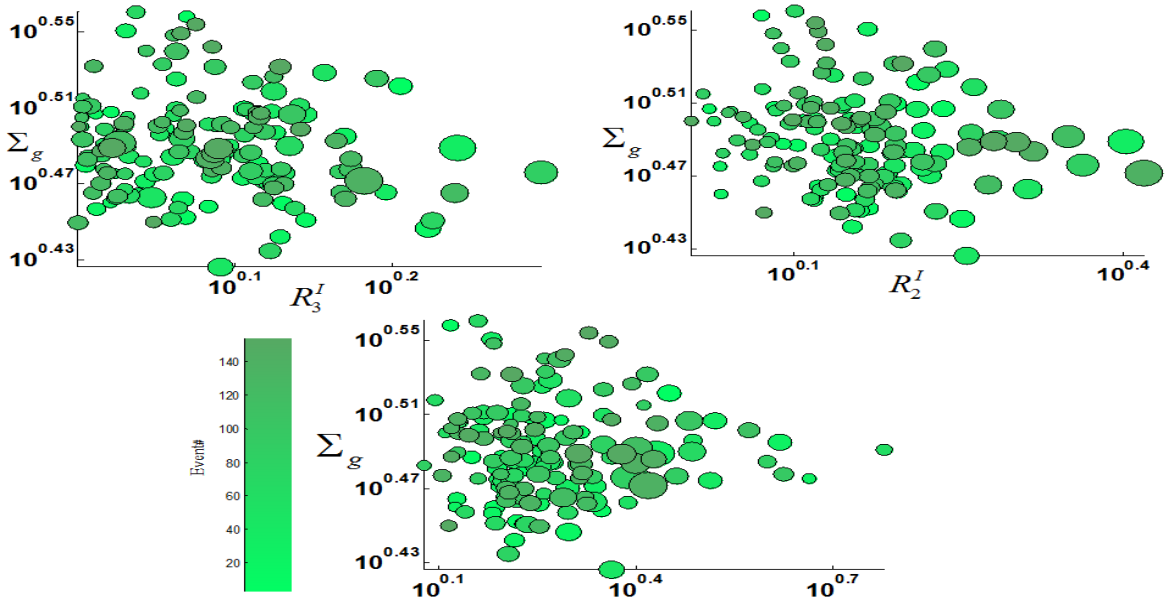

Figure S.16 The average skewness of Q-profiles (Σ_g) versus max. R in each layer.

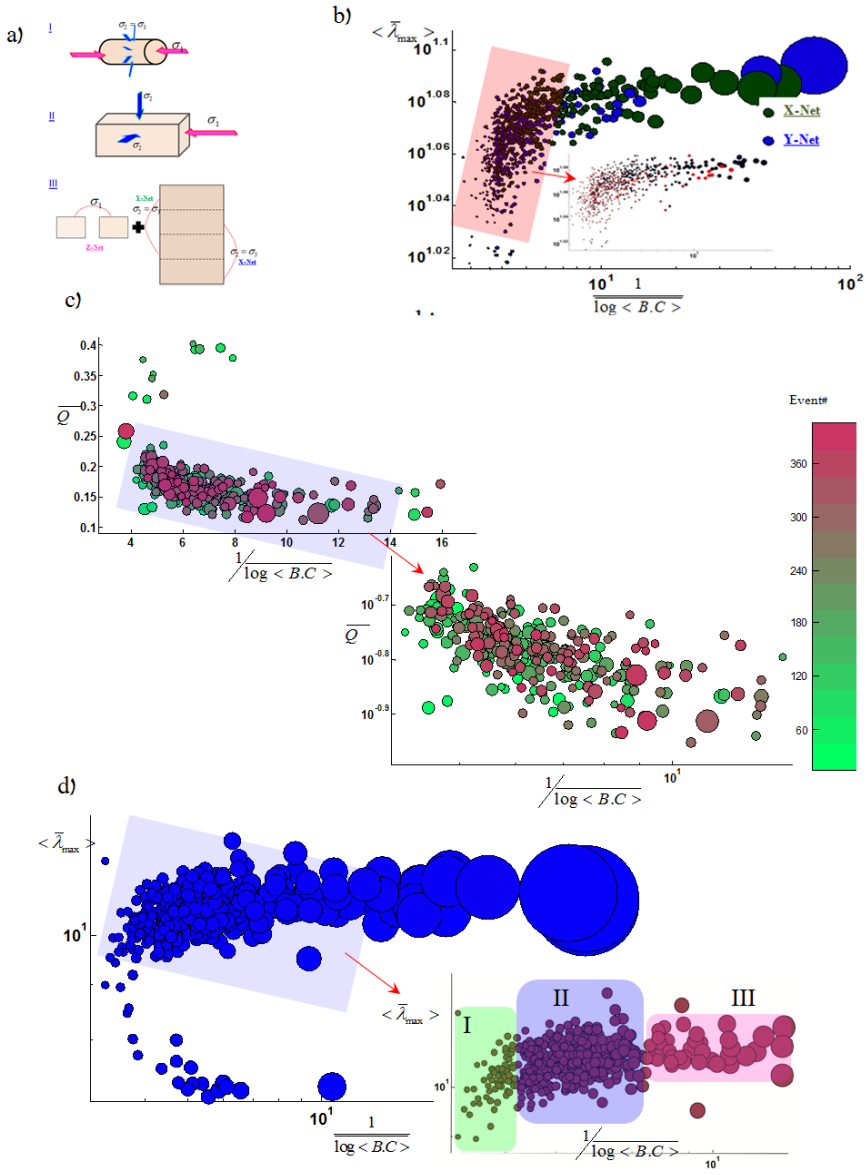

Figure S.17. Global and local networks on CTT. (a) mapping a cylindrical sample to the flatten surfaces. With this technique, we analysze X and Y sub-networks while Z-sub networks are ignored (due to the lack of sensors in corresponding planes) .(b) X and Y layers' phase space shows a much more uniform distribution of events rather than distinguished cluster in TTT's sub-network. (c) The same events from panel (b) in the global networks' metric (all events satisfy $\{R_i^l\}_{i=1,2} > 1$) .(d) ~600 events without considering $\{R_i^l\}_{i=1,2} > 1$ from the CTT test unravel a universal picture of the recorded acoustic events with three main trends. The classified events in the inset of the panel (d) indicates the three main trends of $\overline{\lambda}_{\max.} \sim \overline{\log < B.C >}^{-\chi}$ based on the best fitted power law per each cluster. Most of events allocate the second cluster .For FTB4 ,the trend of this phase plane is different in a way that the first trend is nearly missing and the slop of clusters are steeper (see Fig.S.8b).

4. Further Experimental Results on TTTs

In this section, we present two more results regarding true triaxial experiments to support our results on FTB4 and the proposed approaches. We repeated the same experimental procedure on the same rock material, while changing the intermediate and the minimum driving stress field. For FTB3 and FTB2, the configurations of the driving stress fields are as follows: FTB3 $\sigma_3 = 10, \sigma_2 = 50$ and FTB2: $\sigma_3 = 10, \sigma_2 = 20$. In Fig.s.15, we have compared the duration of the fast slip phase for three TTTs. The duration of the second evolutionary phase while considering identical number of nodes for all cases for FTB3, FTB4 and FTB2 are ~20 μs ,~10 μs and ~10 μs, respectively. To explain the longer duration of FTB3 (which approaches to the CTT because is not a true triaxial test due to the imbalance of forces in this experiment), we compare the $\frac{1}{\log < B.C >_{x,y,z}}$ - $\overline{\lambda}_{\max_{x,y,z}}$ over FTB4 , FTB3 and FTB2 (Fig.S.19). With regard to the approximated power law coefficient in the phase diagram $\overline{\lambda}_{\max.} \sim \overline{\log < B.C >}^{-\chi_i}$, we have for FTB3: $\chi_x \gg \chi_y > \chi_z$ (on average), while for other cases $\chi_y \geq \chi_x \geq \chi_z$. We logically infer that the duration of the second phase is related to the trends of layers in the phase diagram. Thus, micro-cracks with the preferentiality to grow in the xz (or xy) plane imprint a shorter duration.

Overwhelmingly, for the CTT cases the X and Y layers are nearly indistinguishable (Fig.S.17-see discussion section), stating a nearly uniform propagation of fracture.We conclude that the probability of finding short-events and somehow finding some sort of anti-cracks occurring in XZ (or XY) plane is higher than YZ plane; then:

$$\begin{cases} \tau_{II}^{CTT} \approx cte & \sigma_2 = \sigma_3, \\ \tau_{II}^{TTT} \leq \tau_{II}^{CTT} & \sigma_2 \neq \sigma_3 \end{cases}.$$

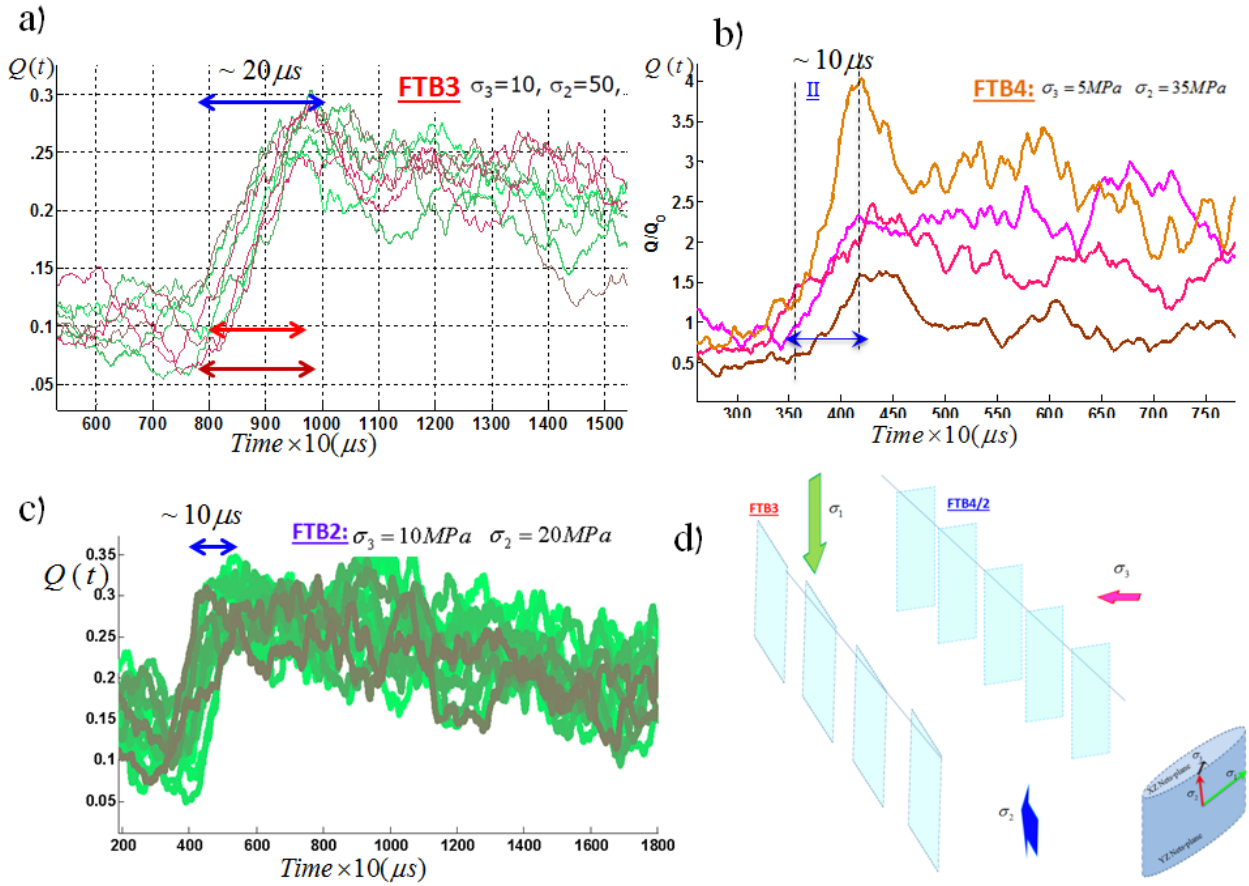

Figure S.18. Time characteristic of fast slip phases for three different true triaxial tests. (a) FTB3 $\sigma_3 = 10, \sigma_2 = 50$ which is 3D stress field but not truly triaxial.' (b)FTB4: $\sigma_3 = 5, \sigma_2 = 35$ and (c) FTB2: $\sigma_3 = 10, \sigma_2 = 20$. (d) Based on the network phase spaces, a schematic presentation of fractures embedded in two planes has been shown. We assume that Z-net is driving the stress field (sigma 1 is the driving force). Events in XZ planes (or the XY plane as quasi-anti cracks) hold a shorter fast-slip phase while rupture fronts in YZ plane allocate longer duration (or normal time-characteristic).

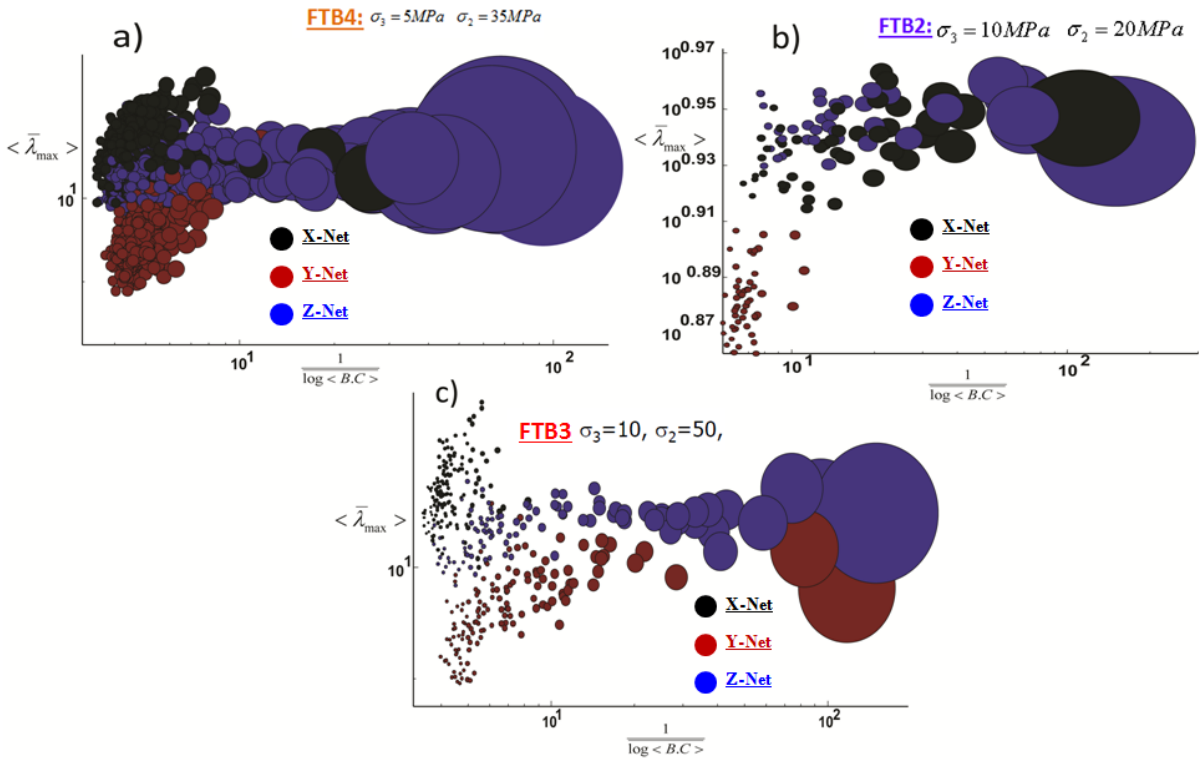

Figure S.19. | Study of sub-networks. Phase diagram of $\bar{\lambda}_{\max}^{x,y,z} - \overline{\log < B.C >}_{x,y,z}^{-1}$ for **(a) FTB4:** $\sigma_3 = 5, \sigma_2 = 35MPa$ **(b) FTB2** $\sigma_3 = 10, \sigma_2 = 20MPa$ **;**.The trends of FTB2 and FTB4' phase spaces are similar ,which is compatible with the similarity of the duration of the fast-slip phase as has been shown in Fig.2a and inset . **(c) FTB3** $\sigma_3 = 10, \sigma_2 = 50MPa$ which is a non-true traixial test**.** Considering a power law such as $\bar{\lambda}_{\max.} \sim \overline{\log < B.C >}^{-\chi_i}$,we have-on average- : $\chi_x > \chi_y > \chi_z$, representing a dominant propagation of rupture fronts in y direction. The size of circles is proportional with the magnitude of $\overline{\log < B.C >}_{x,y,z}^{-1}$. In fact, here we project events into three independent layers. It turns out the trends of X-Y layers are correlated with the duration of weakening time in TTTs [**also see Fig.S1e, Fig.S.6]**.

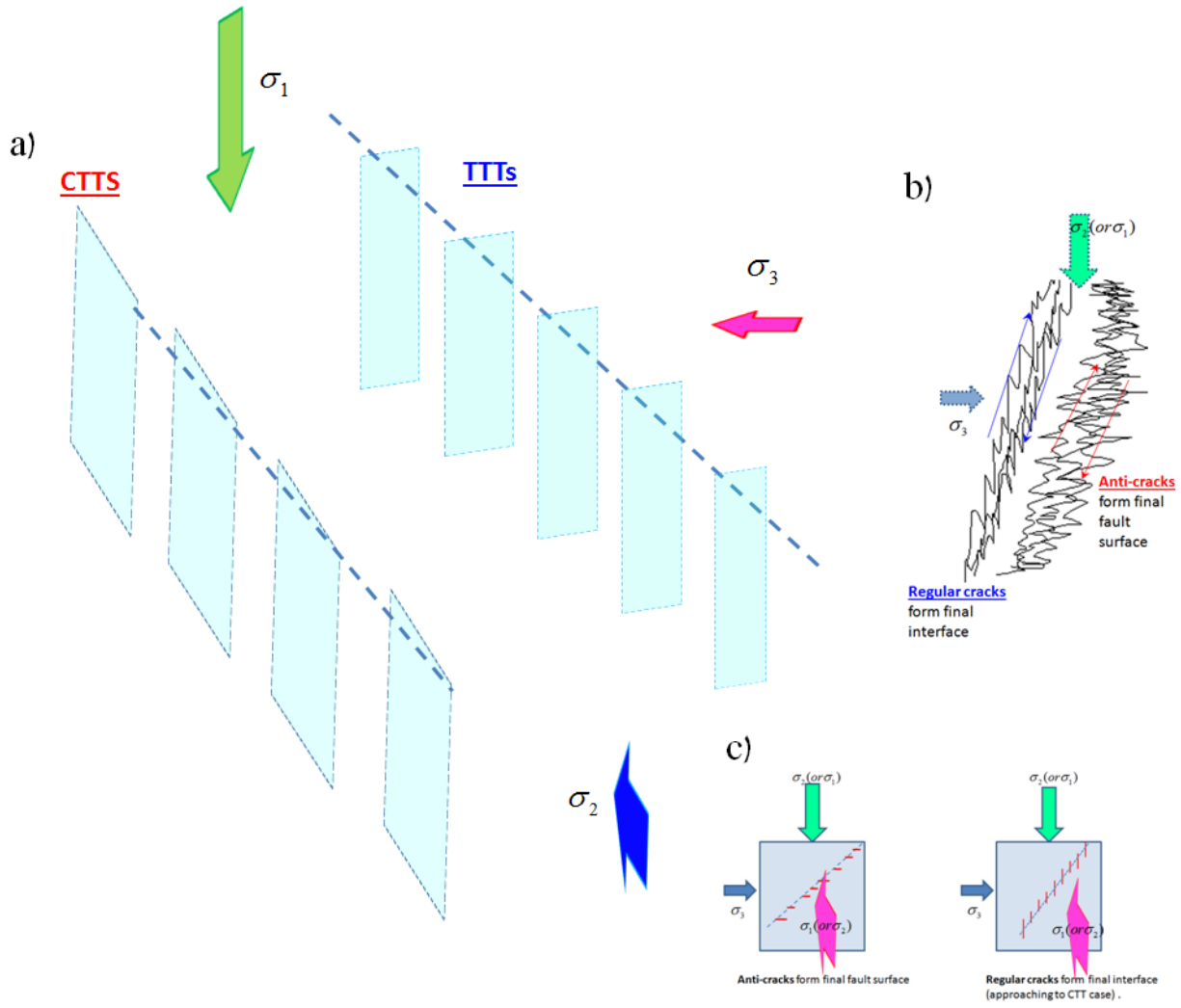

Figure S.20| schematic representations of two model-based regular and irregular cracks' (anti-cracks) interactions to develop a self-organized nucleation of a fault plane. The regular cracks and their interactions have been established through early CTTs and the theory of M-curve proposed in (16-17).

5. Discussion

To compare the TTT's sub-networks and global networks with CTT's functional-networks' features, we use the following technique (considering that a cylinder can be seen an *n-gonal prism* where *n* approaches infinity). We flatten the cylindrical samples and, ignoring the curvature of surfaces, *n* planes plus two circles are produced. Since, in our acoustics set-up, there is no acoustic transducer in the top and bottom of the cylindrical samples, we ignore those two additional top and bottom circular planes (Fig.S.17a). With this mapping, assuming *n=4*, we reach an equivalent scenario to the flattened? cubic (Fig.S.6b). Repeating the same procedure and with the same number of nodes in each layer (here two layers: X and Y), we find a different trend of X-Y sub-networks' phase diagrams (Fig.S.14b). Here, events occupy homogeneously the phase space of $\overline{\lambda}_{\max}$ - $\overline{\log < B.C >}^{-1}$, while in the TTT results Y-networks (pre)dominantly reveal a separated cluster with more sensitivity to the control variable ($\overline{\log < B.C >}^{-1}$). In the scale of the global networks, the range of the networks' parameters are broader than TTT's diagnostics which in turn induces a broader range of the shape of waveforms and then micron/sub-micron rupture regimes (Fig.S.17c &. Fig.S.14b). As a summary to the comparison, we showed that ruptures in the conventional cylindrical experiments may represent more abnormality which can be interpreted in terms of the quality of energy flow into a crack tip.

Next, to analyze patterns of multiplex networks (in this case independent sub-networks) , we use the results of two-well studied experiments on smooth (saw-cut) and rough (natural fault) faults – embedded in the Westerly granite samples (7,18). Similar to the CTT-Sandstone test, we find that X-Y sub networks do not separate in different clusters and nearly all the patterns are uniform in our "standard" network phase space (Fig.S.21).

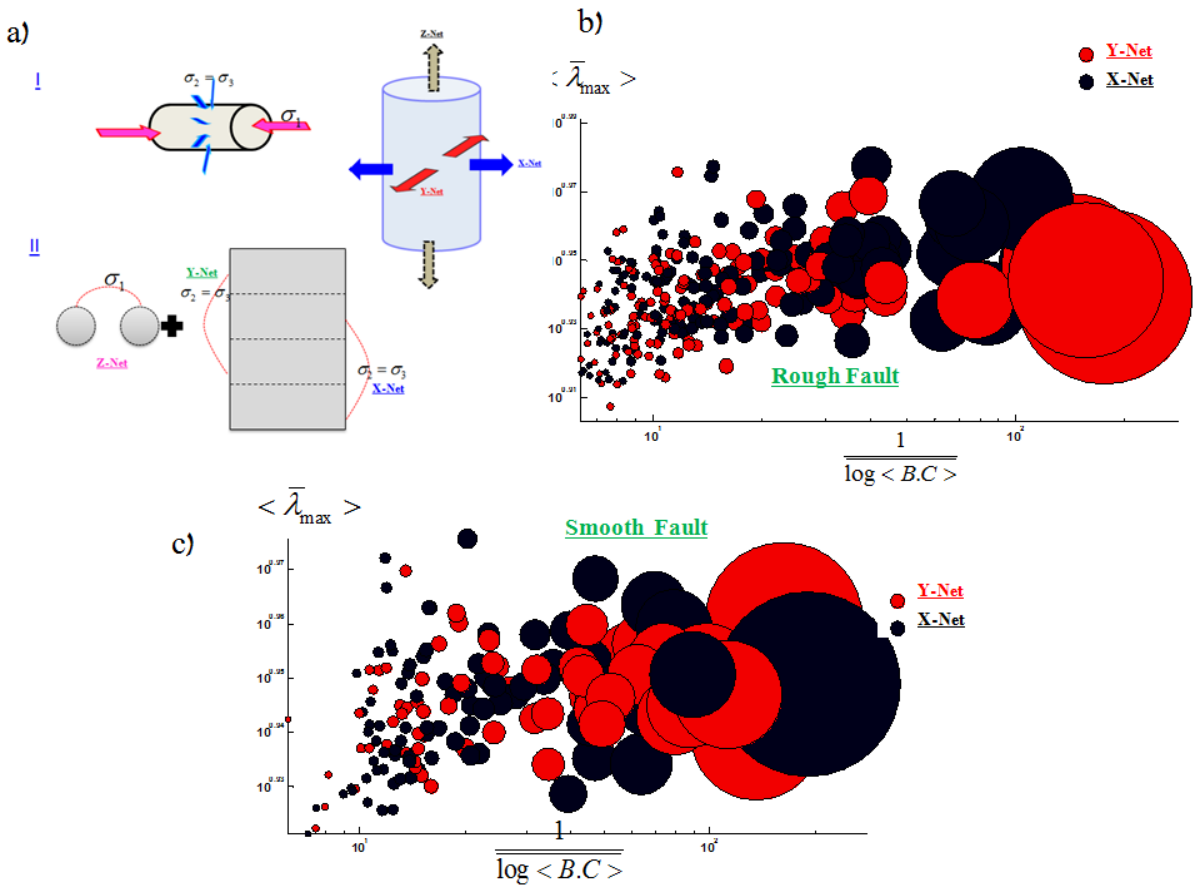

Figure S.21|(b) X-Y sub networks' phase space on events from the naturally made-rough fault (18) (c) Multiplex networks and X-Y sub networks' phase space on events from the embedded saw-cut fault in~60 in Westerly Granite (18) . No significant separation or clusters can be recognized in the $\frac{1}{\log < B.C >_{x,y}}$ - $\overline{\lambda}_{\max_{x,y}}$ plane.

Using events from the saw-cut fault experiment (~100 events in three cycles of stick-slip cycles) and mapping the maximum and minimum R values from each event (from the first phase) ,we find a failure-criterion phase space ,similar to TTT (FTB4) . The results show three distinctive trends in $\Upsilon_R - R_{\max}$ (Figs.22a) : 1) $R_{\max} \to R_{\min}$ which results in an insensitive section of the phase space. (2) $\Upsilon_R \sim R^{\beta}{}_{\max}, \beta > 1$ and (3) a few events occupy: $\Upsilon_R \sim R^{\beta}{}_{\max}, \beta \to 1$.

Thus, (precursory) cracks of smaller length allocate the smaller $R_{\max}$ (phase I). However, approaching the final crack length or main (big) stress drop (stick-slip) will happen in the third section of the phase space.

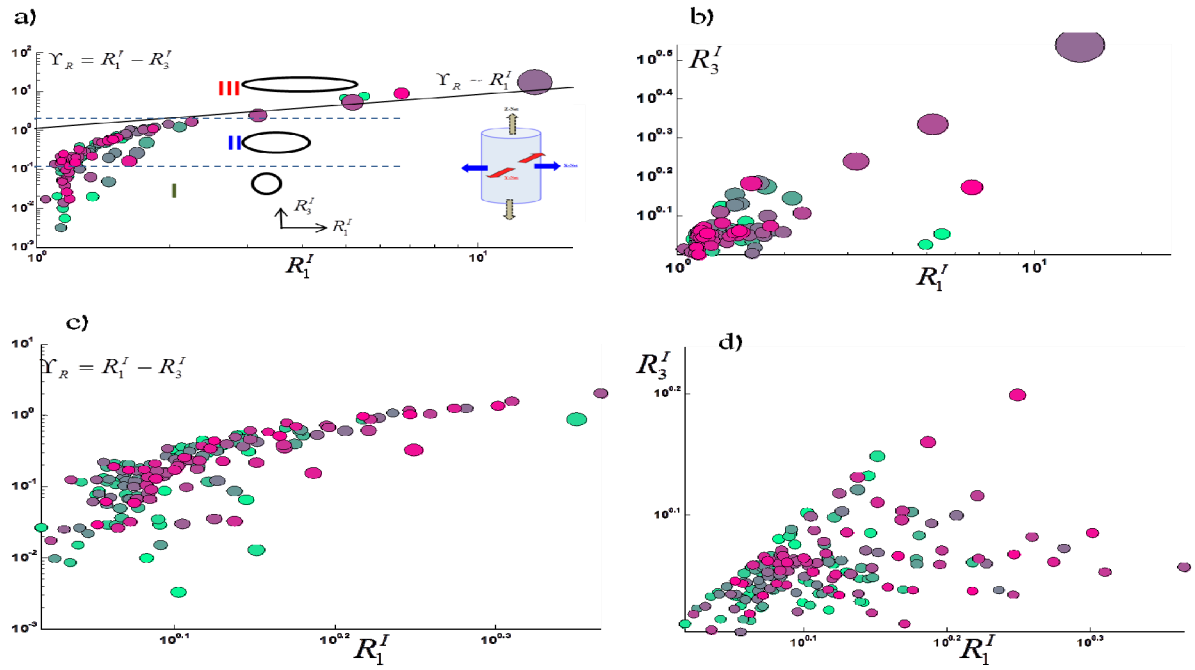

Figure S.22| (a-b) Maximum R values from X and Y sub-networks from a smooth-fault and **(c-d)a** Rough fault**.** The color shows the events' sequence and the size of circles is proportional to the minimum R value.

HP-HT tests: To compare the observed short-phase Q-profiles with most possible anti-cracks, we compare typical anti-cracks' waveforms with TTT's Q-profiles. We set up a global network on a multi-anvil test (accomplished at University College London) on olivine samples. The procedure of the test was similar to (20) with a confining pressure of 2 to 5 GPa and a temperature between 800-1400K. In Fig.S.23, we have shown two typical waveforms and their corresponding Q-profiles (from the deformation phase at ~2GPa), demonstrating an encoded short duration of the second phase <10μs. Since one of the main mechanisms of faulting at high pressure tests is associated with anticrack development (21-22), we claim that the short duration of the second generic phase is due to abnormal cracking (the second phase of Q-profiles from samples under regular CTT lasts ~20-25 μs).

Our observation of a shorter rupture time and a shorter fast-slip phase in a multi-anvil test does coincide with Heidi Houston and Quentin Williams's conclusions (23-24) that many deep events (deep-focus earthquakes) start up significantly faster than do intermediate or shallow events. In

addition, our results from the multi-anvil test confirmed the results of (24) that the entire rupture time of deep-earthquakes (with a possible anti-cracks' origin) is about half that of shallower events. An interesting point is the trend and the details of the evolution of the second phase (Fig.S24). As we have shown the path of the weakening stage is not completely linear .In fact, this path is very similar to the strain hardening of crystals, frequently with three distinguished phases:1) the low-hardening stage; the forest hardening and the slop increases and the decrease in strain hardening rate. Then, we postulate that an event from HP-HT is due to dislocation and that the weakening phase is the result of the complex motion of dislocations. Our results do not distinguish smooth plastic flow (or super-plastic flow) in the fast-slip phase. The extreme plasticity might be identified in the next evolutionary phases of Q-profiles. This matter needs to be investigated in greater detail.

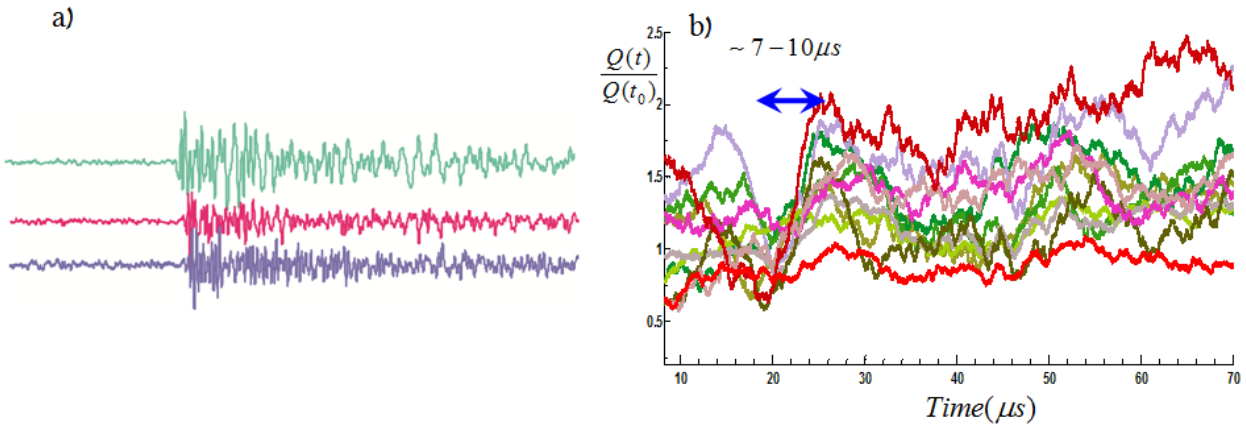

Figure S.23| Typical waveforms and processed Q-profiles proposed to have an origin of anti-cracks in a Multi-Anvil test; We have shown typical waveforms from an event (a) from anti-crack faulting in olivine samples and a collection of 10 events and their corresponding Q-profiles(b). The duration of the second phase is ~<10 μs.

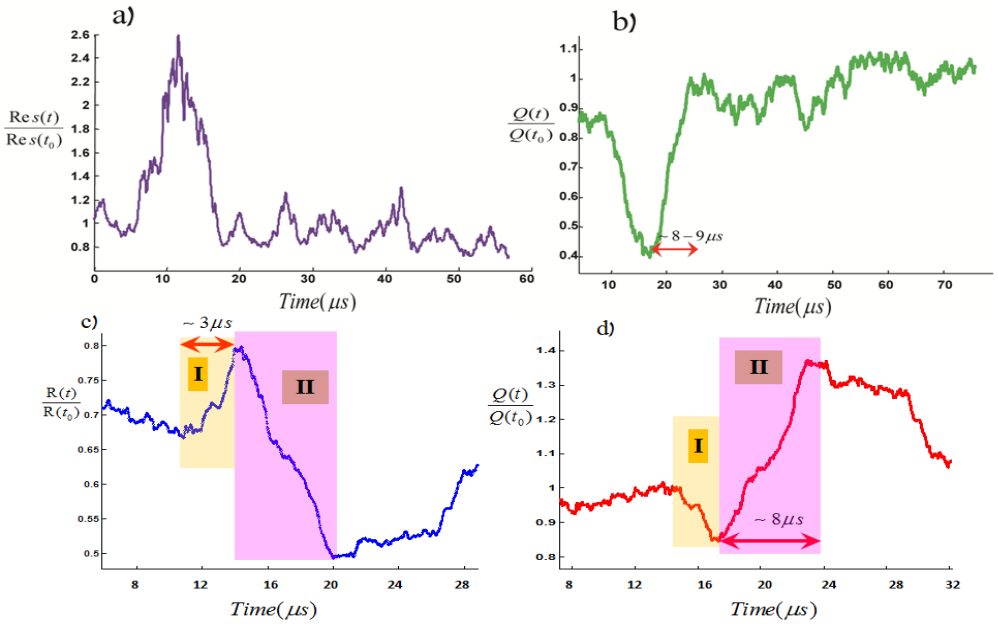

Figure S.24| typical R and Q profiles from two events from the HP-HT test. We highlighted the duration of the first and the second phase

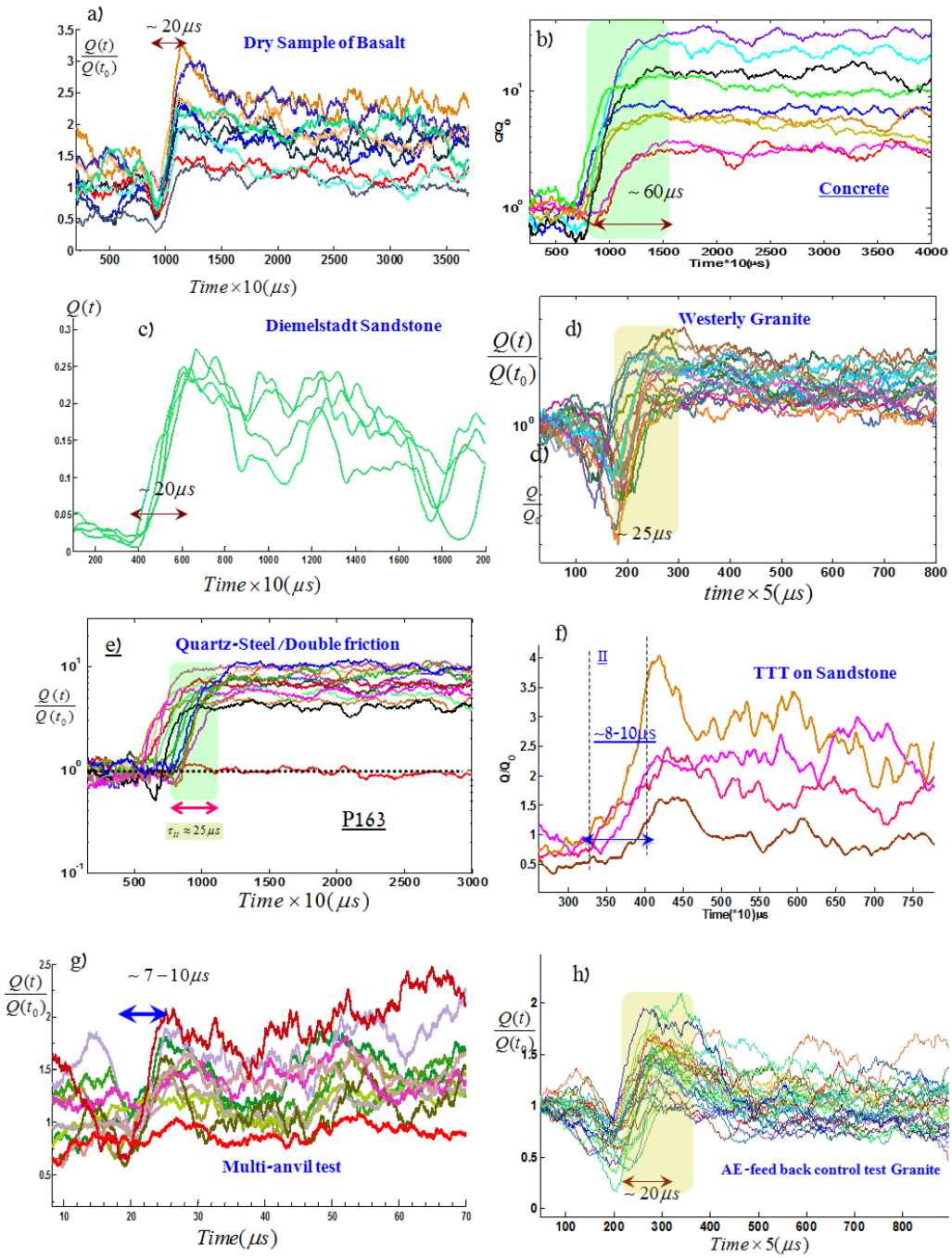

Figure S.25| Summery of studied waveforms from 9-set of experiments on different brittle materials. Our test included simple friction-test, conventional cylindrical triaxial tests, polyaxial tests, High pressure –High temperature, and tests on frictional-gouge interfaces. We used granite, sandstone, basalt, olivine and concrete samples.

References

(1) Young, RP., Nasseri. MHB., & Lombos, L. Imaging the effect of the intermediate principal stress on strength, deformation and transport properties of rock using seismic methods. *Ture triaxial testing of rocks*, CRC Press, Taylor & Francisco Group, Balkema, 167-179 (2013).

(2) Schubnel, A., Thompson, B. D., Fortin, J., Guéguen, Y., & Young, R. P. Fluid□induced rupture experiment on Fontainebleau sandstone: Premonitory activity, rupture propagation, and aftershocks. *Geophysical Research Letters*, 34(19) (2007).

(3) Reches, Z. Faulting of rocks in three-dimensional strain fields. II. Theoretical analysis. *Tectonophysics* 95, 133–156 (1983).

(4) Thompson, B.D,R.P. Young, D.A. Lockner, Fracture in Westerly Granite under AE Feedback and Constant Strain Rate Loading: Nucleation, Quasi-static Propagation, and the Transition to Unstable Fracture Propagation. Pure and Applied Geophysics, 163 (5-6): 995-1019 2006.

(5) Mair, K., Marone, C., & Young, R. P. Rate dependence of acoustic emissions generated during shear of simulated fault gouge. *Bulletin of the Seismological Society of America*, 97(6), 1841-1849 (2007).

(6) Ben-David, O., Rubinstein, S. & Fineberg, J. Slip-Stick: The evolution of frictional strength. *Nature*. 463, 76 (2010).

(7) Ghaffari, H. O., & Young, R. P. Acoustic-friction networks and the evolution of precursor rupture fronts in laboratory earthquakes. *Nature Scientific reports*, 3 (2013).

(8) Katsaga, T., Sherwood, E. G., Collins, M. P., & Young, R. P. (2007). Acoustic emission imaging of shear failure in large reinforced concrete structures. International Journal of Fracture, 148(1), 29-45.

(9) Benson, P. M., B. D. Thompson, P. G. Meredith, S. Vinciguerra, and R. P. Young (2007), Imaging slow failure in triaxially deformed Etna basalt using 3D acoustic-emission location and X-ray computed tomography, Geophys. Res. Lett., 34, L03303, doi:10.1029/2006GL028721

(10) Townend, E., Thompson, B. D., Benson, P. M., Meredith, P. G., Baud, P., & Young, R. P. Imaging compaction band propagation in Diemelstadt sandstone using acoustic emission locations. *Geophysical Research Letters*,35(15) (2008).

(11)) Zapperi, S., Castellano, C., Colaiori, F. & Durin, G. Signature of effective mass in crackling-noise asymmetry. *Nature Phys*. 1, 46–49 (2005).

(12) Mehta, A. P., Mills, A. C., Dahmen, K. A. & Sethna, J. P. Universal pulse shape scaling function and exponents: Critical test for avalanche models applied to Barkhausen noise. Physical Review E. 65 (4), 046139 (2002).

(13) Mogi, K. Fracture and flow of rocks under high triaxial compression. *Journal of Geophysical Research*, 76(5), 1255-1269(1971).

(14) Haimson, B., & Chang, C. A new true triaxial cell for testing mechanical properties of rock, and its use to determine rock strength and deformability of Westerly granite. *Int.J. Rock Mechanics and Mining Sciences*. 37(1), 285-296(2000).

(15) Colaiori, F. (2008). Exactly solvable model of avalanches dynamics for Barkhausen crackling noise. Advances in Physics, 57(4), 287-359.

(16) Reches, Z. & Lockner, D. A. Nucleation and growth of faults in brittle rocks. *J. Geophys. Res*. 99, 18159–18173 (1994)

(17) Healy, D., Jones, R. R. & Holdsworth, R. E. Three-dimensional brittle shear fracturing by tensile crack interaction. *Nature* 439, 64–67 (2006)

(18) Thompson, B. D., Young, R. P. & Lockner, D. A. Premonitory acoustic emissions and stick-slip in natural and smooth-faulted Westerly granite. *J Geophys Res*. 114, B02205J (2009).

(19) Rubinstein, S. M., Cohen, G., & Fineberg, J. (2007). Dynamics of precursors to frictional sliding. Physical review letters, 98(22), 226103.

(20) De Ronde, A. A., Dobson, D. P., Meredith, P. G., & Boon, S. A. (2007). Three□dimensional location and waveform analysis of microseismicity in multi□anvil experiments. Geophysical Journal International, 171(3), 1282-1294.

(21) Green, H. W., Scholz, C. H., Tingle, T. N., Young, T. E., & Koczynski, T. A. Acoustic emissions produced by anticrack faulting during the olivine→ spinel transformation. *Geophysical research letters*. 19(8), 789-792 (1992).

(22) Green, H. W., Young, T. E., Walker, D., & Scholz, C. H. Anticrack-associated faulting at very high pressure in natural olivine. *Nature*.348(6303), 720-722(1990).

(23) Houston, H., & Williams, Q. (1991). Fast rise times and the physical mechanism of deep earthquakes.

(24) Houston, H., & Vidale, J. E. (1994). The temporal distribution of seismic radiation during deep earthquake rupture. Science, 265(5173), 771-774.

(25) Mucha, P. J., Richardson, T., Macon, K., Porter, M. A., & Onnela, J. P. Community structure in time-dependent, multiscale, and multiplex networks. *Science*, 328(5980), 876-878 (2010).

(26) Gao, J., Buldyrev, S. V., Stanley, H. E. & Havlin, S. Networks formed from interdependent networks. *Nature Phys*. 8, 40–48 (2012).

(27) Ghaffari, H. O. & Young, R. P. Network configurations of dynamic friction patterns. *EPL* 98 (4), 48003 (2012).

(28) Ghaffari, H. O. & Young, R. P. Topological complexity of frictional interfaces: friction networks. *Nonlinear Processes Geophys*. 19, 215 (2012).

(29) Newman, M.E.J. *Networks: An Introduction* (Oxford University Press, 2010).